frontiers

# Coast-O-Matic: an automated shoreline detection method using PlanetScope satellite imagery

**Alfred Hewetson** [1,*], **James Lawrence** [1] **and Ioannis Karmpadakis** [1]

[1] *Department of Civil and Environmental Engineering, Imperial College London, London, United Kingdom*

Correspondence*:
Alfred Hewetson
alfred.hewetson19@imperial.ac.uk

## ABSTRACT

Multispectral satellite imagery enables routine surveying of the surf zone by discretising the land–sea interface at known water levels, supporting estimates of coastal recession and accretion. The daily revisit of PlanetScope provides near-continuous shoreline observations, increasing temporal resolution relative to traditional tasking. Many existing approaches delineate shorelines by applying a single spectral index threshold, typically NDWI, and contouring the resulting binary mask. We present an alternative, fully probabilistic method. An ensemble of multilayer perceptrons (MLPs) is trained to predict, for each pixel, the probability of "water" versus "land." The shoreline is then extracted as an isoprobability contour, eliminating the need for a global threshold and allowing spatial variability in sensor response, illumination (e.g., shadows), and local geomorphology to be accommodated. Applied to PlanetScope imagery at Seaford, UK, and evaluated against a height contour referenced to the instantaneous water level, the method achieves a root-mean-square error of $\approx 7\,\mathrm{m}$ for scenes with $<$50% cloud cover. These results indicate that probabilistic pixel-wise classification, coupled with high-cadence PlanetScope acquisitions, offers robust shoreline detection suitable for high-frequency coastal monitoring.

**Keywords: Shoreline detection, Coastal monitoring, Remote sensing, Planetscope, Machine learning**

## 1 INTRODUCTION

Approximately 1.4 billion people live within 25 km of the coast, with over 100 million residing below $1\,\mathrm{m}$ above sea level (Williams et al., 2018; Zhang et al., 2004). Climate change is expected to intensify risks in these areas through accelerated coastal retreat, driven by sea-level rise and changing hydrodynamic conditions such as storm surges and wave–induced storms (Muis et al., 2020; Vousdoukas et al., 2018).

Predicting future shoreline change is critical for effective coastal management. This can be achieved either through numerical modelling or by extrapolating from observed historical trends. However, the development of accurate coastal models is often constrained by a lack of high-quality topographic data for training and calibration (Splinter et al., 2013; Vitousek et al., 2023). Most available data are derived from in-situ surveys or ground-based imagery (Boak and Turner, 2005), which are typically limited in spatial and/or temporal resolution.

The dynamic nature of coastal environments—characterised by both short- and long-term variability—renders traditional survey methods insufficient for continuous monitoring (García-Rubio et al., 2015). Although a few well-monitored sites exist (Larson and Kraus, 1994; McCarroll et al., 2023; Turner et al., 2016), they are too limited in number to provide broad spatial coverage. The growing availability and capability of Earth observation satellites offer a promising alternative for expanding the scope and frequency of coastal data collection (Belward and Skøien, 2015).

Satellite remote sensing has been successfully applied to monitor coastal topography and shoreline change at regional to global scales (Bishop-Taylor et al., 2019; Li and Gong, 2016; Luijendijk et al., 2018). It is increasingly used to bridge the temporal gaps between traditional field surveys, providing a more continuous record of shoreline evolution (Vitousek et al., 2023). Earth observation satellites are broadly categorised into two types: active sensors, which transmit signals and analyse the returned response, and passive sensors, which detect natural radiation emitted or reflected by the Earth's surface (Di and Yu, 2023; ESA Space Solutions, 2020).

Active remote sensing systems, such as LIDAR (Light Detection and Ranging) and SAR (Synthetic Aperture Radar), derive surface elevation by measuring the time delay between the emitted signal and its reflection. One of the most commonly used active satellite systems for coastal studies is Sentinel-1 SAR, which operates independently of cloud cover and sunlight at a typically 10m resolution (Torres et al., 2012). However, it presents several limitations. Its revisit time is approximately 12 days, or 6 days when both Sentinel-1A and 1B are functional (Geudtner et al., 2014). Moreover, generating a digital elevation model (DEM) typically requires at least two acquisitions, effectively reducing the temporal resolution to 24 days under ideal conditions (Braun, 2021). This low frequency can result in the loss of critical morphological changes between acquisitions. In addition, SAR signals do not penetrate water, meaning areas below the high-water line cannot be resolved, especially when images are captured during high tide. This limits SAR's effectiveness in mapping the dynamic nearshore zone, which is often the primary area of interest in shoreline studies.

Despite these limitations, SAR can be used to delineate the shoreline by exploiting the sharp contrast in backscatter between land and water surfaces. When the tidal level at the time of image acquisition is known, the derived shoreline can be interpreted as a water-line contour, and used to infer surface elevation along its length (Mason et al., 1995). Angelini et al. (2025) demonstrated that enhanced preprocessing of high-resolution TerraSAR-X data can achieve a Mean Absolute Deviation (MAD) as low as 2.5 m, while Sentinel-1 datasets consistently yield a MAD $< 7.0$ m on Mediterranean beaches. Furthermore, Savastano et al. (2024) showed that these SAR-derived shorelines are highly robust for monitoring morphological changes, achieving a correlation coefficient ($R^2$) of 0.9 when tracking shoreline movement across diverse coastal environments.

This water-line method can also be applied to passive imagery. Unlike active sensors, passive satellites operate by detecting reflected or emitted energy from the Earth's surface; essentially capturing an image. The pixels in these images can be classified into land and water, allowing the instantaneous shoreline to be defined as the boundary between these two classes (Boak and Turner, 2005; Dolan et al., 1978). As with SAR, if the water level is known, the shoreline position can be used to infer elevation along the coast.

Most passive satellites used for coastal monitoring acquire multispectral imagery, which goes beyond standard RGB (red, green, blue) photography by capturing reflectance across a broader portion of the electromagnetic spectrum. These bands typically span from the visible to the infrared range, enabling improved discrimination between land cover types based on their distinct spectral properties.

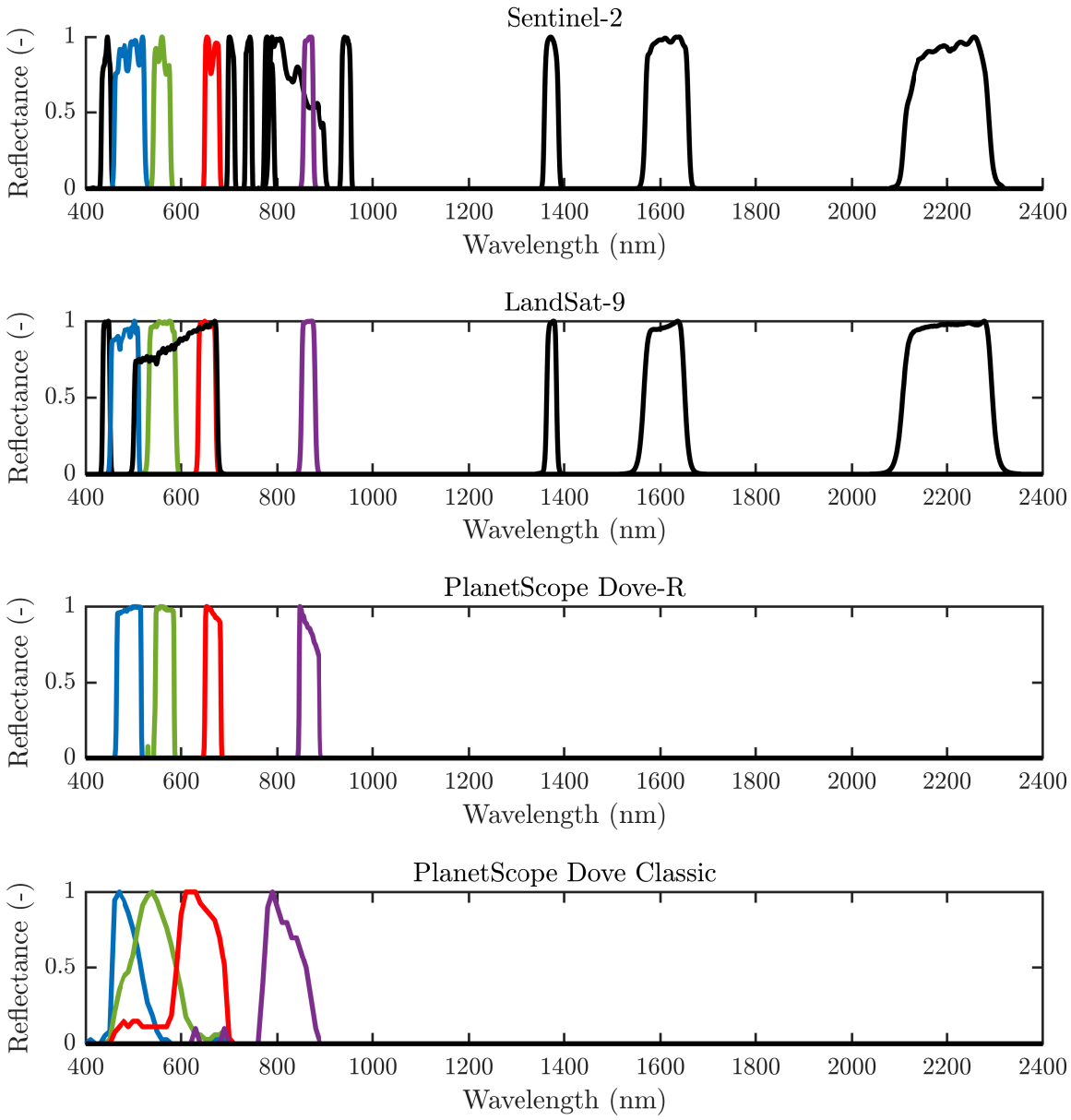



**Figure 1.** Spectral response of satellite sensor instruments. Blue, green and red lines are the respective RGB bands, purple is the NIR band, black bands are additional bands that do not have an equivalent PlanetScope band

The two most widely used public multispectral satellite systems for Earth observation are Landsat and Sentinel-2. The Landsat programme, initiated in 1972 with the launch of Landsat-1, has undergone several upgrades, with Landsat 7, 8, and 9 currently in operation (Wulder et al., 2022). These satellites typically provide imagery at 30 m spatial resolution, with a 15 m panchromatic band, and revisit each location approximately every 16 days. Landsat 8 and 9 offer 11 spectral bands, covering the visible, near-infrared, and short-wave infrared regions. Figure 1 displays the spectral response of each of the bands and illustrates how strongly the sensor responds at each frequency. These bands are used to detect specific reflectance

characteristics associated with different surface types. For instance, Bands 2, 3, and 4 correspond to the blue, green, and red portions of the spectrum, respectively, while additional bands extend into the infrared range, facilitating more nuanced classification.

Sentinel-2, also shown in Figure 1, was introduced in 2015 and currently consists of three satellites, with Sentinel-2C launched in 2024. Each satellite provides a revisit time of 10 days, resulting in a combined effective revisit period of less than 5 days (Phiri et al., 2020; Spoto et al., 2012). Sentinel-2 acquires imagery at 10–20 m resolution, using 13 spectral bands across the visible and infrared spectrum. The increased spectral range available from both Landsat and Sentinel-2 significantly improves the ability to classify surface materials, as different land cover types exhibit distinct reflectance and absorption behaviour at various wavelengths (Roy et al., 2021).

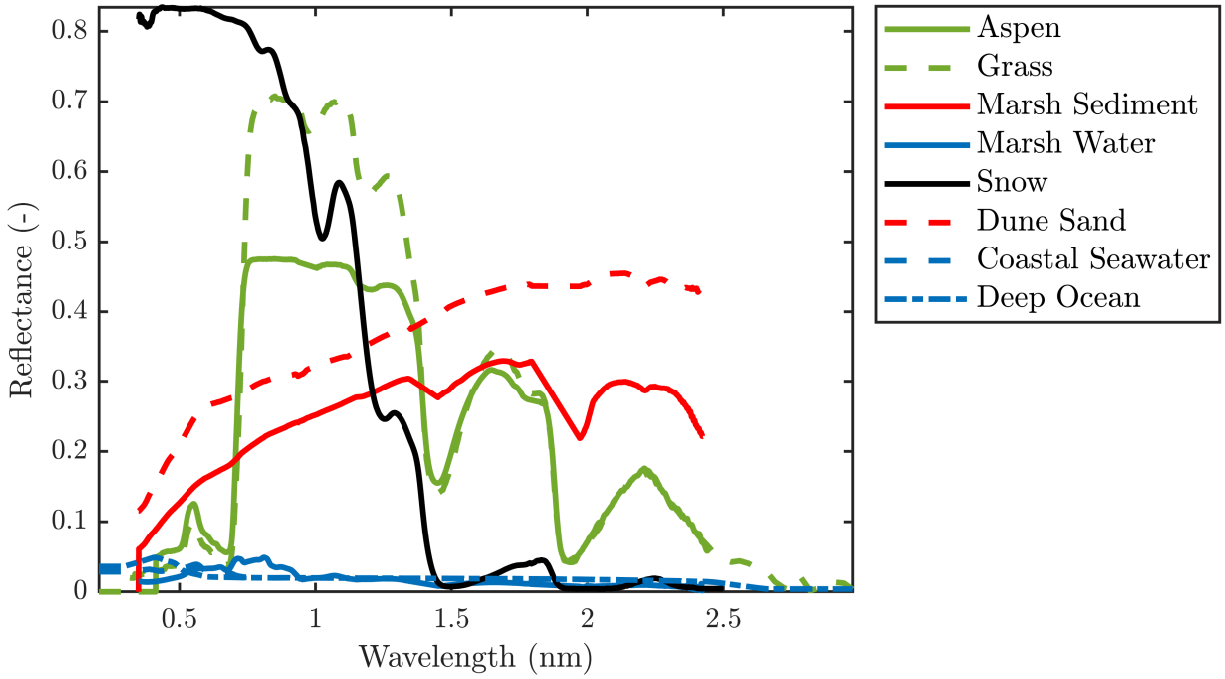



**Figure 2.** Characteristic reflectance of specific classes with respect to wavelength. Green lines are respective of vegetation classes, red lines are geological materials and blue lines are water based classes

A key example is water, which strongly absorbs near-infrared radiation, resulting in low reflectance values in these bands (Rustamov et al., 2018). This behaviour is shown in Figure 2, which shows in the blue water associated lines the reflectance dropping as wavelength increases. Other classes, such as vegetation and soil, exhibit their own spectral signatures More specifically, vegetation shows a sharp rise in the near-infrared, while soil often displays a more linear response across the spectrum. These spectral differences form the basis for a range of band ratio indices that are commonly used in classification tasks.

One such index is the Normalized Difference Water Index (NDWI) (McFeeters, 1996), defined using the green and infrared (IR) bands, as shown in Equation 1.

$$\mathrm{NDWI} = \mathrm{GmIR}_{\mathrm{norm}} = \frac{\mathrm{Green} - \mathrm{IR}}{\mathrm{Green} + \mathrm{IR}} \tag{1}$$

This index enhances water–land separation by exploiting the strong absorption of infrared by water. The use of normalised indices, such as NDWI, also compensates for local lighting variations, including shadows and differences in solar zenith angle at the time of image acquisition (Kriegler et al., 1969; Rouse Jr et al., 1974). Other indices, such as the Normalized Difference Vegetation Index (NDVI), shown in Equation 2, further demonstrate how spectral relationships can be leveraged to distinguish between surface classes in a robust and interpretable manner.

$$\mathrm{NDVI} = \mathrm{IRmR}_{\mathrm{norm}} = \frac{\mathrm{IR} - \mathrm{Red}}{\mathrm{IR} + \mathrm{Red}} \tag{2}$$

When applying the water-line method, the differences between active and passive satellite imagery are primarily twofold. First is the ability to acquire cloud-free observations. Active sensors such as SAR can penetrate cloud cover and are unaffected by solar illumination, enabling consistent imaging during adverse weather or at night. This provides a significant advantage over passive systems, which are often obstructed by cloud and haze. However, SAR data can be highly noisy, particularly in the nearshore zone where surface roughness and water dynamics interfere with signal interpretation as discussed by (Salameh et al., 2020). Consequently, the clarity of shoreline detection using SAR is often compromised, despite its all-weather capability.

The second key difference lies in temporal resolution. Sentinel-1, an active radar system, achieves a best-case revisit interval of 6 days when both satellites in the constellation are operational. This is comparable to the revisit time of Sentinel-2, a passive multispectral system with a combined constellation return period of approximately 5 days. However, recent advances in the commercial satellite sector have led to the deployment of new constellations that offer significantly higher temporal frequency and, in some cases, improved spatial resolution.

A prominent example is Planet's PlanetScope constellation, comprising over 180 CubeSats known as Dove and SuperDove satellites. First launched in 2014, PlanetScope is capable of capturing imagery at daily intervals with a spatial resolution of approximately 3.7 metres (Planet Labs PBC, 2023). The small size and standardised CubeSat design of these satellites facilitate mass production and deployment. Combined with the use of off-the-shelf sensors, this approach significantly reduces the cost and complexity of satellite launches (Safyan, 2020), making high-frequency Earth observation more accessible.

Despite these advantages, the spectral capabilities of PlanetScope satellites are more limited than those of public missions like Sentinel-2. The original Dove satellites capture only four spectral bands—Red, Green, Blue, and Near-Infrared (RGBI), a relatively narrow portion of the electromagnetic spectrum, indicated in Figure 1. This restricts the discriminative power of pixel classification due to the reduction in available information as well as the range that this information spans on the spectrum. Particularly in environments where multiple land cover types exhibit overlapping spectral responses. The newer SuperDove satellites have expanded this capacity by including four additional bands. However, even with this improvement, the spectral range remains significantly narrower than Sentinel-2's 13-band configuration, which spans both visible and shortwave infrared regions.

The classification of PlanetScope imagery is further complicated by inconsistencies in image quality, arising from both geometric and radiometric issues (Frazier and Hemingway, 2021). Geometric inaccuracies are primarily caused by variability in the spatial alignment of ground features across images. These discrepancies result from the internal positioning errors of the satellites and the absence of consistently reliable ground control points. While Planet reports a positional accuracy of less than 10 m RMSE at the

$90^{\text{th}}$ percentile (Planet Labs PBC, 2023), independent studies have shown greater variability. For example, Dobrinić et al. (2018) report an RMSE of $6.41\,\mathrm{m}$ with a maximum offset of $11.85\,\mathrm{m}$, while Houborg and McCabe (2018) observed errors of up to $19\,\mathrm{m}$. Such spatial offsets pose significant challenges to applications requiring high precision, such as sub-pixel shoreline extraction.

Radiometric inconsistencies across PlanetScope datasets arise from two main sources. The first is the evolution of the satellite hardware. Planet initially deployed the Dove Classic (PS2) satellites, followed by Dove-R (PS2.SD) in 2019 and the SuperDove (PSB.SD) series in 2020 (Planet Labs PBC, 2023; PBC, 2021). Each generation brought improvements in image quality, but also introduced shifts in spectral band placement, leading to inconsistencies within long-term datasets (Huang and Roy, 2021). These differences are visualised in the two different PlanetScope rows of Figure 1, which shows the spectral response of two different generations of PlanetScope satellites. The PS2 Dove classic shown in Figure 1 shows but one variant, (ID_0e), with there also being a small variation also across this generation.

The second major source of radiometric variability is the lack of on-board calibration systems, which distinguishes PlanetScope from larger platforms like Sentinel-2 and Landsat. Due to the CubeSat form factor, these satellites cannot carry internal calibration modules. Instead, calibration is performed externally, using lunar reflectance comparisons and cross-sensor validation with RapidEye and Landsat 8 at established calibration sites (Collison et al., 2022; Wilson et al., 2017). While effective to an extent, this results in a radiometric uncertainty of approximately 5–6%. Some studies have reported even higher variability in specific bands; for instance, Tu et al. (2022) observed errors of 8% in the red and infrared bands, with an uncertainty margin of 9%. In comparison, Landsat 8 and Sentinel-2 maintain radiometric uncertainties around 3% (Lamquin et al., 2019; Markham et al., 2014), reflecting more robust calibration protocols.

A third limitation, common to most passive satellite systems, is the effect of atmospheric conditions, particularly clouds, haze, and shadows, which degrade image quality and complicate classification. Cloud detection is inherently challenging, and this is exacerbated in PlanetScope imagery by its reduced spectral range, which lacks the thermal and shortwave infrared bands that facilitate cloud and haze identification in platforms like Sentinel-2 and Landsat (Roy et al., 2021). The consequences of these limitations are evident in Figures 2 and 1, which compare the spectral coverage and class separation of PlanetScope with broader-band satellites. The practical impact of this is that the presence of shadow ,thin clouds or haze can significantly distorts the spectral response and undermines classification accuracy.

To mitigate this, PlanetScope imagery includes a Usable Data Mask (UDM), which identifies pixels affected by clouds and shadows, as described in Planet Labs PBC (2023). In 2018, this was upgraded to UDM2 to improve detection performance (Keay et al., 2023). However, the accuracy of these masks remains uncertain (Roy et al., 2021), particularly in identifying thin or diffuse clouds, and residual artifacts often persist, introducing errors in downstream applications such as shoreline extraction.

When applying the shoreline detection method, each satellite image yields a single piece of cross shore information: the location where the waterline intersects a transect. While this provides only an instantaneous snapshot, the spatial and temporal resolution of the imagery significantly influences the method's effectiveness. In this context, PlanetScope offers two main advantages over publicly available satellite platforms such as Sentinel-2 and Landsat.

The first advantage lies in its higher spatial resolution. Although there is debate in the literature regarding the benefits of increased resolution for the detection of linear features, such as shorelines. Cipolletti et al. (2012) notes that resolution improvements do not always lead to enhanced accuracy, and earlier studies have highlighted issues such as metrication errors in quantised images (Kulpa, 1983; Vossepoel and Smeulders,

1982), more recent work suggests otherwise. For example, Doherty et al. (2022) compared shoreline detection accuracy across satellite platforms and found a clear improvement with higher pixel resolution. Similarly, Hagenaars et al. (2018); Kelly and Gontz (2019); Pardo-Pascual et al. (2014) all concluded that the resolution of input imagery imposes a fundamental constraint on the precision of shoreline extraction, particularly when attempting sub-pixel or near-pixel level delineation.

The second key advantage of PlanetScope is its temporal resolution. Unlike Sentinel-2 (5-day revisit) or Landsat (16-day revisit), PlanetScope can provide daily imagery, enabling the capture of short-term coastal processes such as post-storm recovery, tidal variability, or rapid morphological change. As da Silva et al. (2024) argue, infrequent satellite observations may fail to resolve transient events and can underrepresent the dynamic nature of many coastal environments. Thus, the high revisit frequency of PlanetScope is essential for capturing a more complete picture of shoreline evolution.

The waterline method has been widely adopted to monitor shoreline change, and its application has been systematically evaluated across multiple algorithms by Vos et al. (2023). In their benchmark study using Sentinel-2 and Landsat imagery, five state-of-the-art algorithms were assessed. Two of these, ShorelineMonitor (Luijendijk et al., 2018) and HighTide-SDS (Mao et al., 2021), derive shorelines from composite images constructed by stacking multiple Landsat acquisitions. These composites are then thresholded using a percentile-based approach applied to specific spectral indices: the Normalized Difference Water Index (NDWI) for ShorelineMonitor and the Automated Water Extraction Index (AWEI) for HighTide-SDS (Feyisa et al., 2014). By averaging multiple images over time, these methods aim to capture the mean sea-level shoreline, under the assumption that tidal fluctuations are uniformly distributed across the composite period. This allows for long-term shoreline recession and accretion trends to be inferred from a smoothed shoreline representation.

The remaining three algorithms evaluated, CoastSat (Vos et al., 2019), SHOREX (Palomar-Vázquez et al., 2018), and CASSIE (Almeida et al., 2021),rely on individual satellite images to estimate instantaneous shoreline positions, which are inherently influenced by the tidal and wave conditions at the time of acquisition. The CASSIE algorithm uses a multilevel Otsu thresholding technique (Otsu, 1979) applied to the NDWI index to generate a binary land–sea classification. This binary map is subsequently refined to sub-pixel resolution by smoothing the pixel boundary interface. In contrast, SHOREX applies a threshold to the AWEI index to define an initial boundary mask. A kernel-based polynomial surface fitting is then employed within a region of interest to estimate a sub-pixel shoreline based on inflection points in the fitted surface. Finally, CoastSat adopts a supervised classification strategy to distinguish between sand and water pixels. The resulting distributions are discretised using Otsu thresholding, and the shoreline is extracted via a marching squares algorithm, which permits continuous shoreline delineation.

The performance of these algorithms is known to be location-dependent, with accuracy varying based on local coastal morphology, tidal range, sediment type, and image quality. Nevertheless, all three models demonstrate the ability to achieve sub-pixel shoreline resolution relative to the spatial resolution of the satellite imagery used. In addition to its evaluation in the benchmark study by Vos et al. (2023), the CoastSat method has been extended by Doherty et al. (2022) to incorporate PlanetScope imagery. When applied to Narrabeen Beach (Australia) and Duck (USA), the method achieved root mean square errors (RMSEs) of $3.5\,\mathrm{m}$ and $>5\,\mathrm{m}$, respectively. These results represent a notable improvement over typical Landsat- or Sentinel-2-based estimates, which often exceed $9\,\mathrm{m}$. However, it is important to note that the PlanetScope implementation of CoastSat did not achieve sub-pixel accuracy relative to PlanetScope's native $3.7\,\mathrm{m}$ resolution, suggesting the difficulties of fully capitalising on the improved spatial resolution of commercial imagery.

With the daily revisit rate of PlanetScope satellites, the available imagery is expanding rapidly. Consequently, several studies beyond Doherty et al. (2022) have sought to harness this temporal density for shoreline detection. Kelly and Gontz (2019) reported an RMSE of approximately $9\,\mathrm{m}$ along the Australian coast, attributing a significant portion of this error to initial geolocation inaccuracies. In contrast, Abdelhady et al. (2022) demonstrated that by comparing satellite-derived shorelines to high-resolution LiDAR surveys, the majority of extracted pixels fall within a single-pixel ($3\,\mathrm{m}$) distance. Similarly, Angelini et al. (2024) achieved sub-pixel accuracy in monitoring complex megacusp undulations in Spain and Italy. However, unlike the systematic approach in Doherty et al. (2022), these studies typically rely on a more curated selection of images and select dates, necessitating a higher degree of manual supervision and data pre-processing.

A common limitation among the shoreline detection methods discussed is their reliance on a single spectral index, such as NDWI or AWEI, to threshold each image into binary land and sea classifications. While effective in many cases, this approach inherently restricts the spatial precision of shoreline extraction. A fixed threshold may perform well in one region of an image but fail in another due to spatial heterogeneity in beach appearance. Variability in shadows, beach debris, sand composition, moisture content, and the presence of man-made structures can all alter pixel reflectance, leading to misclassification. This limitation is particularly pronounced in UK coastal environments, where irregular morphologies, urban infrastructure, and frequent overcast conditions introduce additional complexity and noise to the imagery.

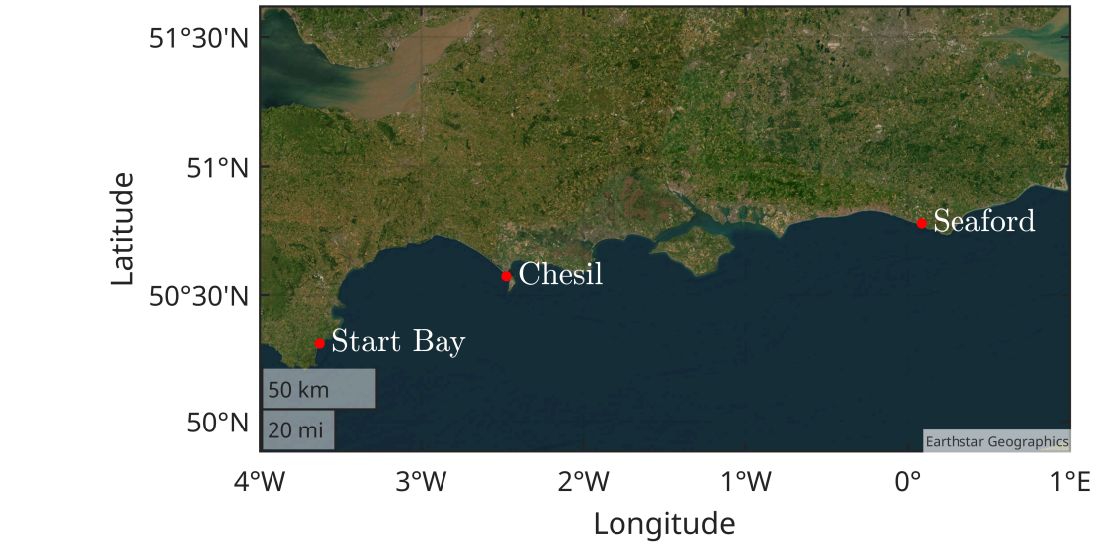
For this reason we develop a methodology that retains the efficiency and interpretability of index-based shoreline detection, while allowing for spatially adaptive classification along each transect. This is achieved through a probabilistic framework, where the shoreline is inferred from a land–sea probability of each pixel rather than a fixed threshold. By estimating the probability of each pixel belonging to land or sea, the method enables sub-pixel shoreline extraction that adapts to local conditions, improving robustness in challenging and heterogeneous coastal settings.

## 2 METHODS AND DATA

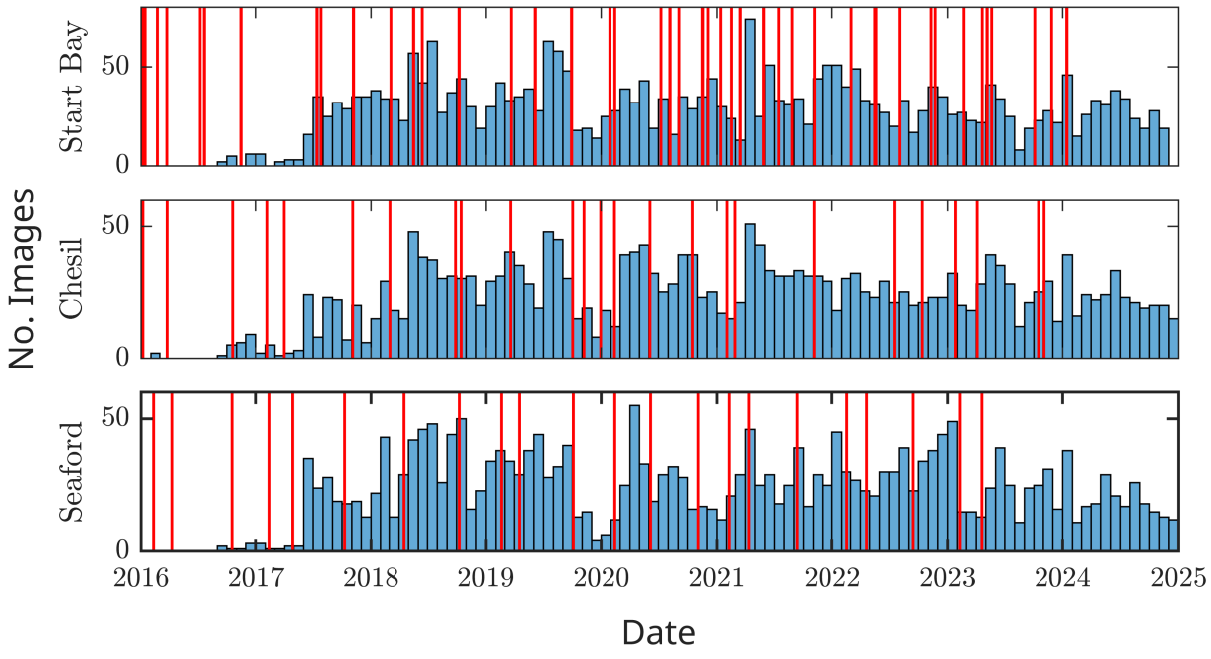
The ultimate objective of this classification process is to estimate the probability that each pixel belongs to either a land or sea class. In this framework, certified sea pixels are assigned a probability value of 1, and those classified as land are assigned a value of 0. Pixels located at the land-sea interface, where class membership is uncertain, are expected to have intermediate values. A contour drawn at the 0.5 probability threshold, representing equal likelihood of land and sea, can then be used to delineate the shoreline at sub-pixel resolution, enabling more precise shoreline extraction than traditional binary classifications. For this, an appropriate classifier needs to be trained that returns this as an output.

In this study, the classifier was constructed using three coastal sites in the United Kingdom: Seaford, Chesil, and Start Bay, shown in Figure 3 A. All three sites are located along the south coast of England and are classified as reflective beaches with predominantly shingle compositions (Konstantinou et al., 2023; Scott et al., 2011; Shanehsazzadeh and Holmes, 2007). The dataset includes 190 surveys and 2579 images from Seaford, 208 surveys and 2934 images from Start Bay, and 45 surveys and 2559 images from Chesil. These images range from mid-2016 when PlanetScope first made images available to the end of 2024, all with a cloud cover percentage under 50%. The distribution of images and the corresponding shoreline surveys for each site is illustrated in Figure 3 B.

The full workflow with the trained classification is shown in Figure 4. The first step is the collection of the images from the Planetscope *analytic udm2* product bundle, which are orthorectified Top of Atmosphere




**(A)**




**(B)**

**Figure 3.** Study site overview and data availability. **(A)** Locations of the three study sites: Start Bay, Chesil, and Seaford along the south coast of England. **(B)** Temporal distribution of the PlanetScope satellite imagery (blue bars) plotted against the dates of in-situ topographic surveys (red lines) for each location.

(TOA) radiance and have been clipped to the area of interest. Before the images are ingested into the model two steps are taken to pre-process the images. The first is the radiometric correction, using PlanetScopes metadata to transform the radiance values to TOA reflectance values.

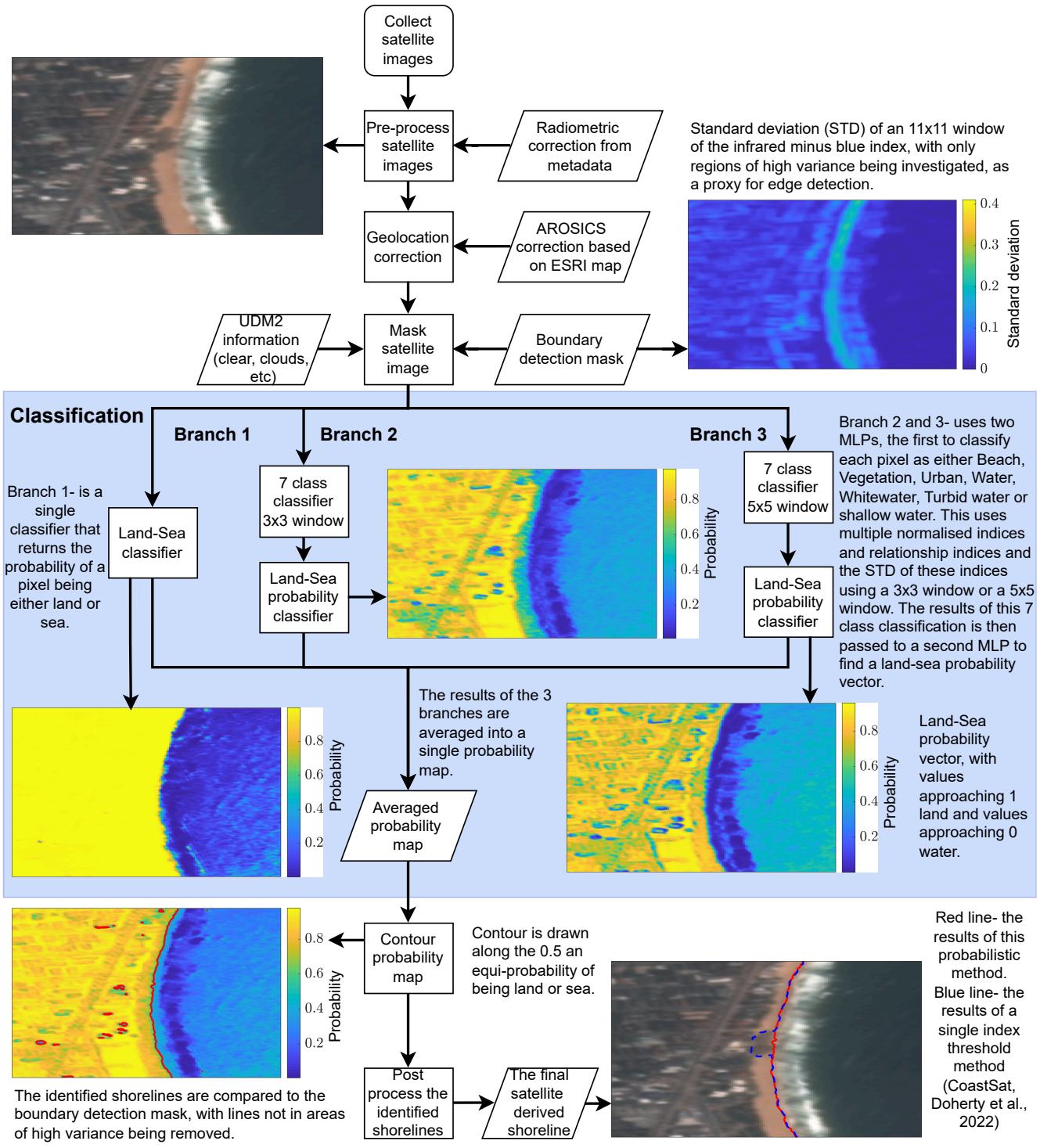



**Figure 4.** Workflow of the Coast-O-Matic algorithm

The second phase of the preprocessing is the geometric correction of the images. For this AROSICS, a Python package designed for sub-pixel image co-registration, is used (Scheffler et al., 2017). AROSICS has been successfully used in similar PlanetScope-based shoreline studies (Doherty et al., 2022; da Silva et al., 2024). However, in this work the area of interests cover a larger area than a single Planetscope image; meaning geolocation based on a single Planetscope reference image is not appropriate due to the possible non-overlapping areas. Therefore, the georeference is based on the ESRI global satellite base map (Esri, 2025), which has been rescaled to the same resolution as Planetscope. This allows all the individual images to be referenced to the same continuous image.

The ESRI satellite basemap utilized the ESRI Vantor Vivid basemap (Vantor, 2024), which maintains a global absolute accuracy of 5 m CE90. Aligning all acquisitions to this unified reference ensures that geolocation errors manifest as a systematic, continuous bias rather than random noise. The automated pipeline for image co-registration and retrieval via the Planet API is available in the GitHub repository of this work.

The final of the sections encapsulates the Coast-O-Matic methodology. First, the per pixel classification, followed by the shoreline identification and finally the masking and post processing. These steps are outlined in more detail below.

## 2.1 Training data

A suitable and representative dataset is essential for training the proposed shoreline classifier. This data was collected by analysing the three UK beaches of Chesil, Start Bay and Seaford.

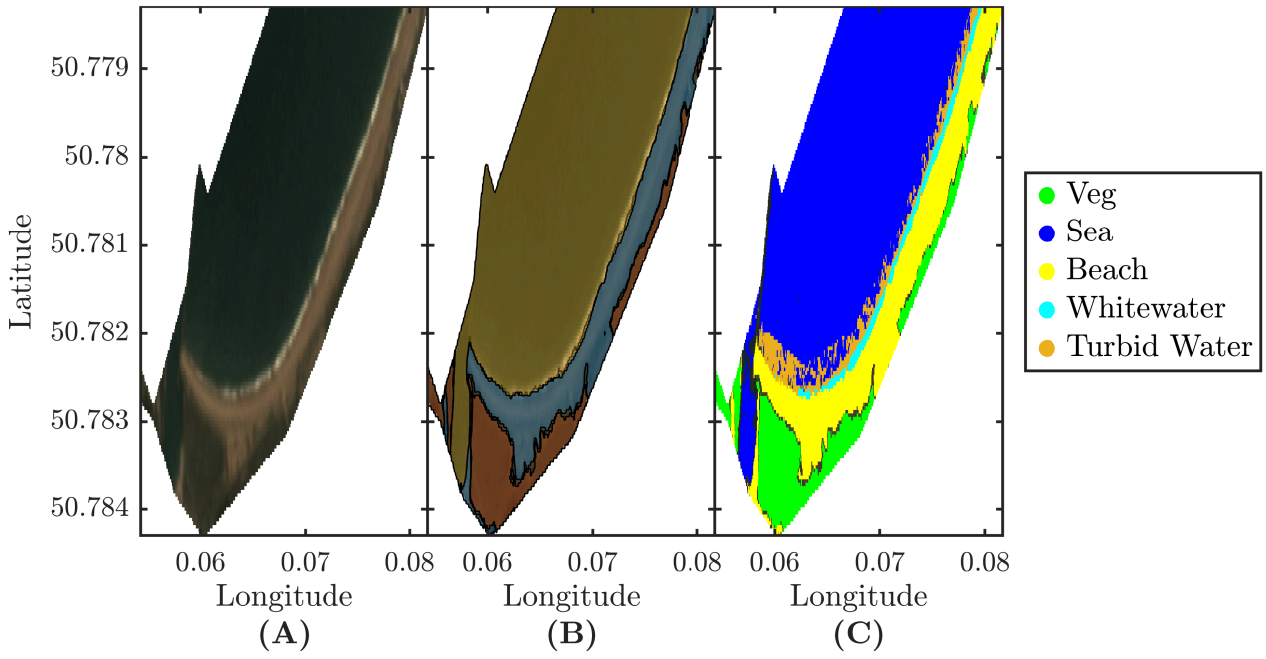



**Figure 5.** Example of data collection from an individual image of Seaford. **(A)** subplot show the raw true colour image (TCI). **(B)** subplot shows the three area that are discretised: water, vegetation and sand. **(C)** subplot shows the pixels that have been assigned to each variable: blue-water, yellow-beach, green-vegetation, turquoise-whitewater, brown-turbid water

Within each region of interest, pixels are categorised into four primary land cover types: water, beach, urban and vegetation. To enhance classification performance, the water class is further subdivided into normal water, turbid water, and whitewater. This additional granularity is introduced for two key reasons. First, it reduces intra-class variability, thereby improving the classifier's ability to differentiate between spectral patterns. Second, it emphasises the nearshore zone, where wave activity commonly generates both turbid water and whitewater through sediment suspension and breaking waves (Hagenaars et al., 2018). This distinction is important because the majority of water pixels in a given image typically represent deeper offshore water, which, if left undifferentiated, can dominate training and reduce sensitivity to the dynamic processes occurring near the shoreline. The challenge is further compounded by the spectral similarity between turbid water and beach pixels in the RGB bands. In shallow or sediment-rich waters, the infrared (IR) band can also be affected by reflection from the seabed or wet sand, further complicating discrimination between land and sea classes (Kalacska et al., 2022). To address this, each image is manually inspected. A loose bounding region is drawn around visible whitewater, and within this area, bright pixels are labelled as whitewater, while darker pixels are classified as turbid water. This process assumes that areas of active turbulence caused by wave breaking exhibit both high reflectance (whitewater) and strong sediment suspension (turbid water), each with distinct but overlapping spectral characteristics.

An example of this discretisation is shown in Figure 5. Figure 5A presents a true colour image (TCI) of Seaford Beach, composed of the RGB bands, with an associated infrared band also available. Figure 5B shows the three core classification regions, sand, sea and vegetation, used in all Seaford images to spatially bin the pixels. Although not shown in this figure, the additional whitewater and turbid zones are drawn manually for each image. Figure 5C illustrates the final pixel classification used for training the model, incorporating all defined subclasses.

To further refine the classification, each of the three primary classes; water, beach, and vegetation are subdivided into five visibility-based subcategories: clear, shadow, hazy, cloud, and dark. The first four are derived from the PlanetScope Usable Data Mask (UDM), which identifies pixels affected by atmospheric conditions or illumination effects. A pixel located within both a class region (e.g., beach) and a UDM-flagged area (e.g., shadow) is assigned the appropriate subclass (e.g., shadow beach). The additional dark class refers to pixels that are consistently misclassified by the model during training. These pixels are flagged and reused for retraining to mitigate classification biases. The term "dark" for these misclassified pixels is due to the majority of them coming from areas of low-reflectance, which commonly leads to classification errors.

A shallow water class is included to address a systematic bias in shoreline detection. Without this class, pixel-based methods tend to show a seaward offset in the extracted shoreline position. This occurs because shallow water pixels often exhibit spectral signatures closer to sand than to deeper water, due to light penetration and reflectance from the seabed. Explicitly modelling shallow water as a distinct class improves the accuracy of shoreline delineation by preventing such misclassifications along the land–sea boundary.

The training dataset comprises individual pixels, each labelled and associated with spectral information from four bands: Red (R), Green (G), Blue (B), and Infrared (IR). To enrich the feature space and accelerate training, a set of 12 input metrics are used, as detailed in Table 1. Among these, three band difference indices are computed (denoted by $m$). For example, Equation (3) captures the difference between the infrared and green bands as:

$$\mathrm{IRmG} = \mathrm{IR} - \mathrm{Green} \tag{3}$$

**Table 1.** List of indices used in the training dataset

| Difference bands | Normalised bands | STD 3x3 window | STD 5x5 window |
|---|---|---|---|
| IRmR | $IRmR_{norm}$ | $IRmR_{norm\ std3}$ | $IRmR_{norm\ std5}$ |
| IRmG | $IRmG_{norm}$ | $IRmG_{norm\ std3}$ | $IRmG_{norm\ std5}$ |
| IRmB | $IRmB_{norm}$ | $IRmB_{norm\ std3}$ | $IRmB_{norm\ std5}$ |
| | | $IRmR_{std3}$ | $IRmR_{std5}$ |
| | | $IRmG_{std3}$ | $IRmG_{std5}$ |
| | | $IRmB_{std3}$ | $IRmB_{std5}$ |

These metrics have previously been shown to enhance class separation in coastal environments (Doherty et al., 2022; Harley et al., 2019).

Additionally, three are normalised spectral indices (subscript $norm$), such as:

$$\text{IRmG}_{\text{norm}} = \frac{\text{IR} - \text{Green}}{\text{IR} + \text{Green}} \tag{4}$$

These are derived from the work of Kriegler et al. (1969) and Rouse Jr et al. (1974), who demonstrated that normalisation reduces sensitivity to illumination effects such as shadowing or variable solar zenith angle.

To further improve class discrimination, the local variability in key spectral features is also considered. Specifically, the standard deviation (std) of the IR-based normalised and difference indices is computed using both $3 \times 3$ and $5 \times 5$ pixel moving windows. This captures texture-based information within the spatial context of each pixel. Prior work by Vos et al. (2019) demonstrated that local variance is particularly effective for identifying sand pixels, which often exhibit distinct spectral variability relative to other classes.

## Multilayer Perceptron - MLP

The classification is performed using multiple Multi-Layer Perceptrons (MLPs) operating independently. An MLP is a type of feedforward neural network consisting of an input layer, one or more hidden layers, and an output layer. Each layer consists of neurons that compute a weighted sum of the inputs from the preceding layer, as defined by:

$$z = \sum_{i=1}^{n} w_i x_i + b \tag{5}$$

This weighted sum is passed through an activation function, such as the logistic sigmoid, given by:

$$\sigma(x) = \frac{1}{1 + e^{-x}}, \tag{6}$$

to produce the neuron's output. The use of multiple layers enables the MLP to capture complex, non-linear relationships in the data, while the activation function introduces the necessary non-linearity for learning intricate decision boundaries.

The output of an MLP is not a probability in the strict statistical sense, but rather a set of coefficients that reflect the model's confidence in a pixel belonging to a given class. In this study, these coefficients are interpreted as pseudo-probabilities, with the outputs across all classes normalised to sum to one. This allows for a probabilistic interpretation of class membership and supports the extraction of a sub-pixel shoreline by

identifying the 0.5 contour along the land–sea boundary, where the classifier is equally uncertain between the two classes.

While explicitly probabilistic models—such as Bayesian networks—have been investigated for shoreline detection, they were found to be more sensitive to noise, particularly in lower-quality images. In contrast, MLPs offer greater robustness across a broader range of image conditions, while still enabling a probabilistic interpretation suitable for fine-resolution shoreline extraction.

## Classification

Image classification in this framework is performed by averaging the outputs of three independently trained classifiers, given schematically in Figure 8. Each classifier corresponds to a distinct branch in the model architecture, designed to capture different aspects of land–sea discrimination while compensating for one another's limitations.

Branch 1 is a binary classifier, an MLP trained to distinguish between land and sea. In this case, the land class comprises both beach (sand) and vegetation pixels, while the sea class includes normal water and turbid water. This classifier uses only the infrared's relationship and normalised indices; the first two columns of Table 1, to try and distinguish water and non-water pixels, omitting the whitewater class to reduce model complexity and minimise noise. Its goal is to provide a robust and generalised probability map for coarse land–sea separation.

As noted by Vos et al. (2019), the local variance of a pixel relative to its neighbouring pixels can be an effective discriminator for certain classes; particularly sand, which typically exhibits low spectral variability. This variance-based information can be leveraged to enhance the performance of a classifier. The approach presented in this study builds upon this concept but applies it differently: rather than using variance to identify sand pixels, it utilises the standard deviation within a moving window as a proxy for edge detection, specifically to identify the boundaries of water bodies.

This method involves computing the standard deviation of spectral indices across a $5 \times 5$ pixel moving window, with particular emphasis on the infrared minus blue (ImB) difference. This index highlights transitions between land and water by exploiting their contrasting spectral properties in these bands. As illustrated in Figure 6, the resulting standard deviation map reveals a distinct boundary along the land–water interface, providing a valuable feature for delineating shorelines with improved spatial precision.

Branches 2 and 3 are more detailed, each comprising a seven-class MLP classifier trained to distinguish between beach, vegetation, urban, water, whitewater, turbid water, and shallow water. These classifiers output a seven-dimensional probability vector for each pixel. The output is then passed through a secondary MLP, which transforms the seven-class output into a land–sea probability. This transformation enables consistent integration with Branch 1, facilitating a unified final probability map. The key difference between Branch 2 and Branch 3 lies in the contextual features used during training: while both rely on infrared-based metrics and normalised indices; the first two columns of Table 1, Branch 2 incorporates the standard deviation of these indices using a $3 \times 3$ moving window, column 3, whereas Branch 3 uses a $5 \times 5$ moving window, column four of Table 1. This design enables each branch to respond differently to local texture and edge information, helping to balance sensitivity and stability across varied coastal conditions.

The purpose of using three parallel classifiers is to mitigate individual model biases and enhance classification robustness, especially in nearshore environments. An example of this bias is the seaward offset of Branch 1, as shown in Figure 7B, which displays the probability outputs relative to the final satellite derived shoreline for an image of Narrabeen beach. This bias is due to this branch struggling to

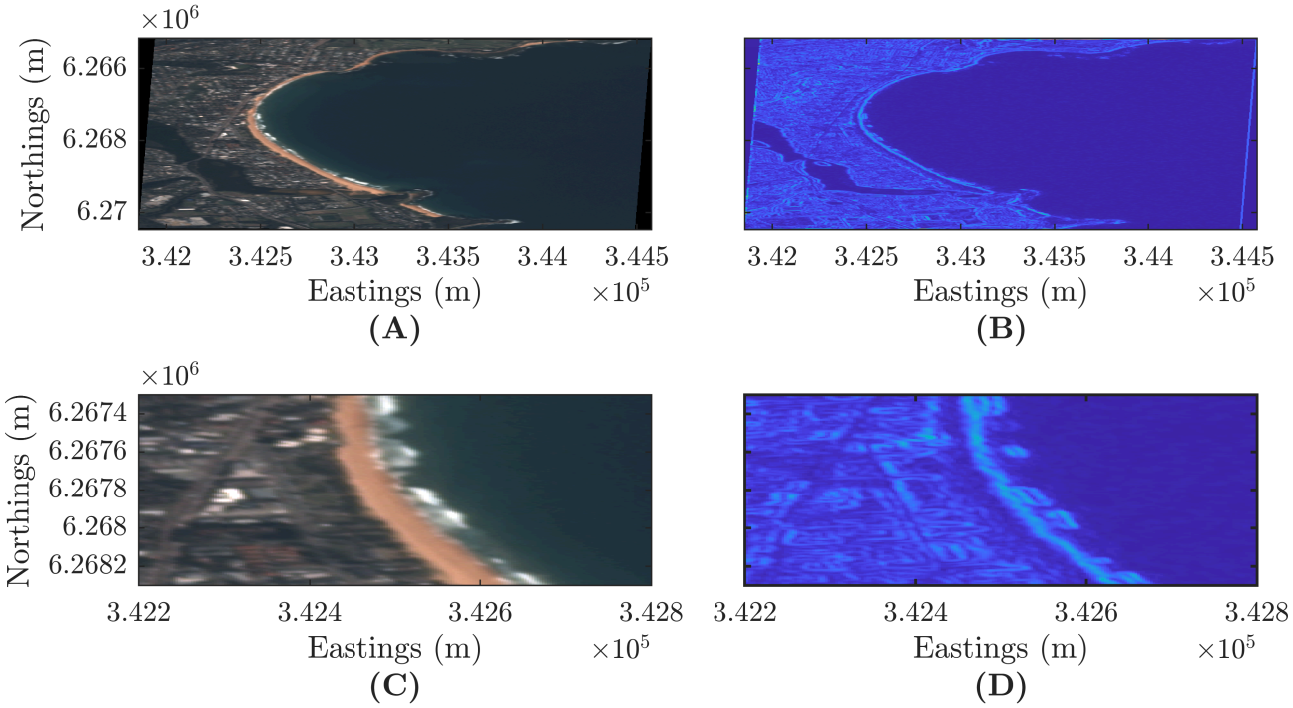



**Figure 6.** Comparison between a true colour image (TCI) of Narrabeen and the associated standard deviation of the infrared minus Blue (IRmB) using a 5x5 moving window

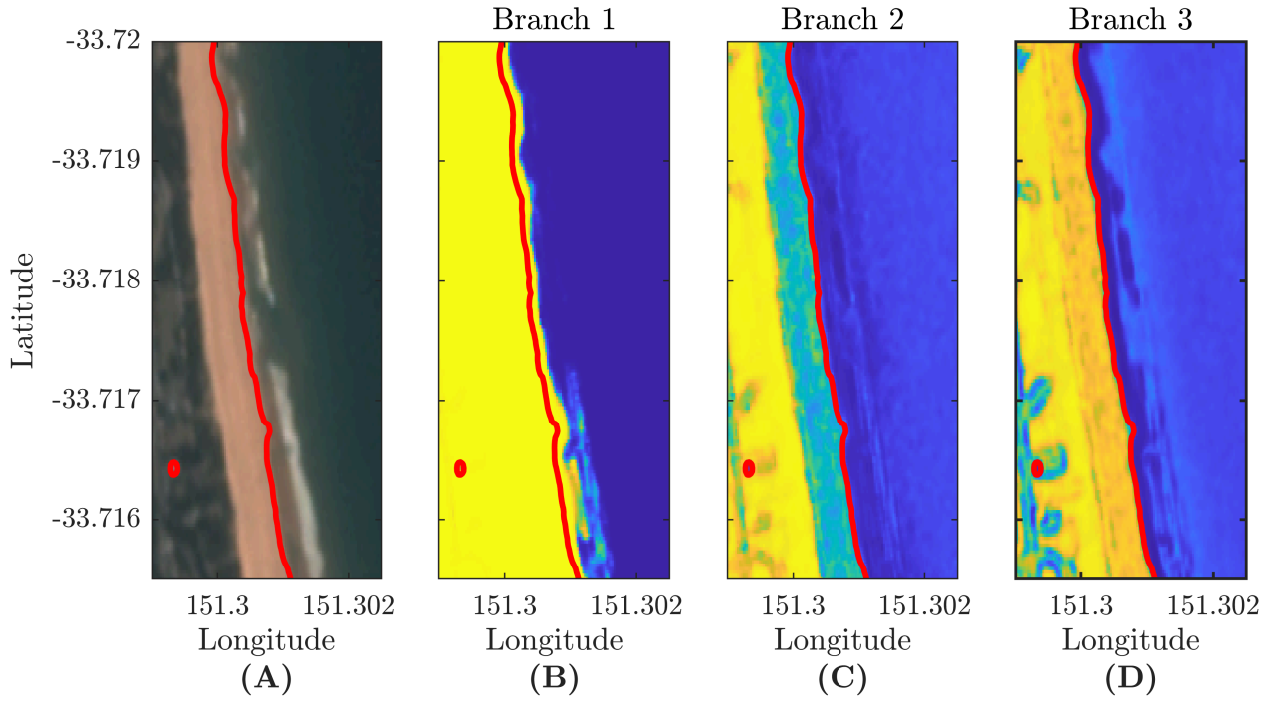



**Figure 7.** This shows the classification results of individual branches on an individual image. **(A)** is the true colour image (TCI of Narrabeen. **(B)** land-sea probability of the first branch. **(C)** probability of the second branch. **(D)** probability of the third branch.

identify whitewater and shallow water features. However, Branch 1 consistently delivers stable land–sea segmentation across a range of visibility conditions.

In contrast, Branches 2 and 3 demonstrate stronger performance in the nearshore zone, particularly in identifying complex features like whitewater, turbid and shallow water, as shown in Figure 7C and 7D respectively. By averaging the outputs, the framework allows the robust global classification of Branch 1 to be refined locally by the more sensitive, high-resolution insights from Branches 2 and 3.

### MLP Training

The classification framework utilizes an ensemble of Multi-Layer Perceptrons (MLPs) optimized for land-sea discrimination through a structured training and resampling strategy. To ensure robust performance across diverse atmospheric conditions, each MLP was initially trained using an equal distribution of pixels from the clear, shadow, hazy, and cloudy sub-classes. Following initial testing within the Coast-O-Matic algorithm, shorelines that exhibited poor performance were resampled to define a ”dark” class, which characterizes pixels with low-reflectance that typically lead to misclassification. The final training set maintained an equal distribution of pixels across all five sub-classes: clear, shadow, hazy, cloudy, and dark.

To maintain classification balance, all binary classifiers were trained using an equal number of sea and land pixels. Within this balanced set, the specific classes constituting land (beach, vegetation, and urban) and sea (normal water, turbid water, whitewater, and shallow water) were also equally distributed.

The architectural specifications vary by branch to balance stability and sensitivity. The Branch 1 binary classifier consists of a single hidden layer with two neurons; it employs a tanh activation function for the hidden layer and a softmax activation function for the output layer. In contrast, all MLPs in Branches 2 and 3,including both the seven-class and binary classifiers,feature a single hidden layer of 12 neurons. These branches utilize the logistic activation function for both hidden and output layers, as defined in Equation 6.

For all model components, the training process was executed using a gradient descent algorithm with a mean square error loss function. The implementation follows the multilayer perceptron methodology provided by Gafford (2026). For further information, regarding weights, biases and hyperparameters, the MLPs themselves are included in the github listed below.

## Border Segmentation and Post-Processing

To derive the shoreline, the fully classified probability map is discretised along the 0.5 isoline. This contour represents the transition where a pixel is equally likely to be land or sea, allowing the boundary to be delineated at sub-pixel resolution. An example of this initial extraction, prior to refinement, is shown in Figure 8.

Following extraction, standard post-processing filters are applied to ensure morphological consistency. The shoreline is cross-referenced with the PlanetScope Usable Data Mask (UDM) to remove segments compromised by cloud cover. A minimum length constraint is also imposed to eliminate fragmented noise that does not represent a continuous coastline.

A more complex challenge arises in built-up coastal areas, where urban structures often exhibit high spectral variance. Since the ”shallow water” class is trained to recognize similar high-variance features, the model can occasionally misclassify inland urban areas as nearshore water, as demonstrated by the small red circle over the built-up area in Figure 8. To distinguish the true shoreline from these inland anomalies, an additional spectral stability metric is applied. Shoreline segments are only retained if they lie within regions of high local variance, defined by the standard deviation of the infrared-minus-blue (IRmB) index over an

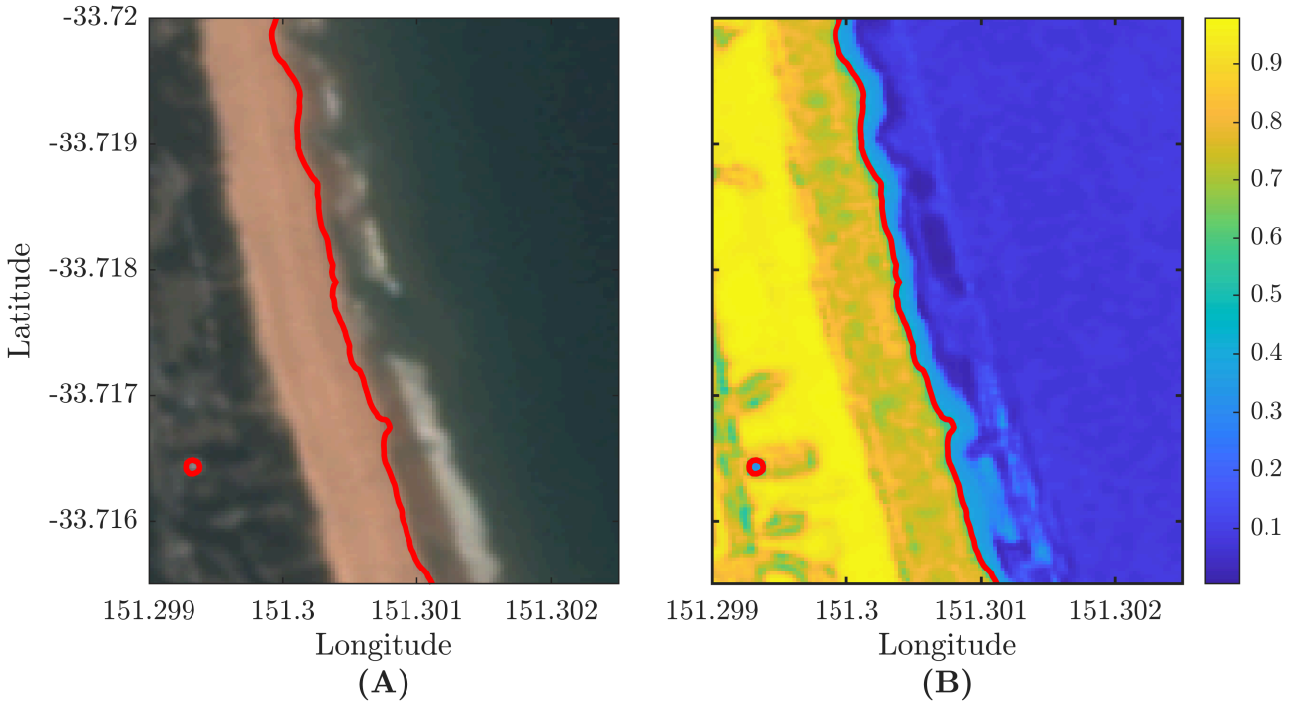



**Figure 8.** **(A)** True colour image (TCI) of Narrabeen showing the equiprobable isoline in red. **(B)** Land–sea probability map including the same isoline.

$11 \times 11$ moving window. By requiring this local deviation to exceed the image-wide mean, the algorithm effectively filters out spurious detections while preserving the strong spectral interface at the water's edge.

Finally, the algorithm imposes a directional constraint by identifying the shoreline from the seaward side. This ensures that the boundary progresses landward from open water, capturing the true interface rather than inland features.

## Model validation

To evaluate the performance of the proposed shoreline detection method, satellite-derived shorelines were validated against both in-situ topographic survey data and results from the PlanetScope version of the CoastSat framework (Doherty et al., 2022). Validation was conducted at the three UK beaches used in training—Seaford, Chesil, and Start Bay—allowing for a direct assessment of generalisation and model accuracy under familiar site conditions.

The CoastSat algorithm was applied using its default configuration, with one key modification: the distance from the reference shoreline. In CoastSat, users are required to manually draw an expected shoreline position, and the algorithm restricts the derived shoreline to a specified distance from this reference. While the default threshold is $40\,\mathrm{m}$, a $100\,\mathrm{m}$ buffer was used in this study. Although this distance exceeds the expected horizontal shoreline variability for the sites, based on their tidal ranges and beach slopes, it was adopted to enable a more inclusive and meaningful comparison between CoastSat and the proposed method, particularly in anticipation of applying these approaches in more complex or dynamic coastal environments with a larger horizontal range.

To quantify the performance of each shoreline detection method, the satellite derived shorelines were compared directly to ground-truth topographic survey data carried out by regional monitoring programs

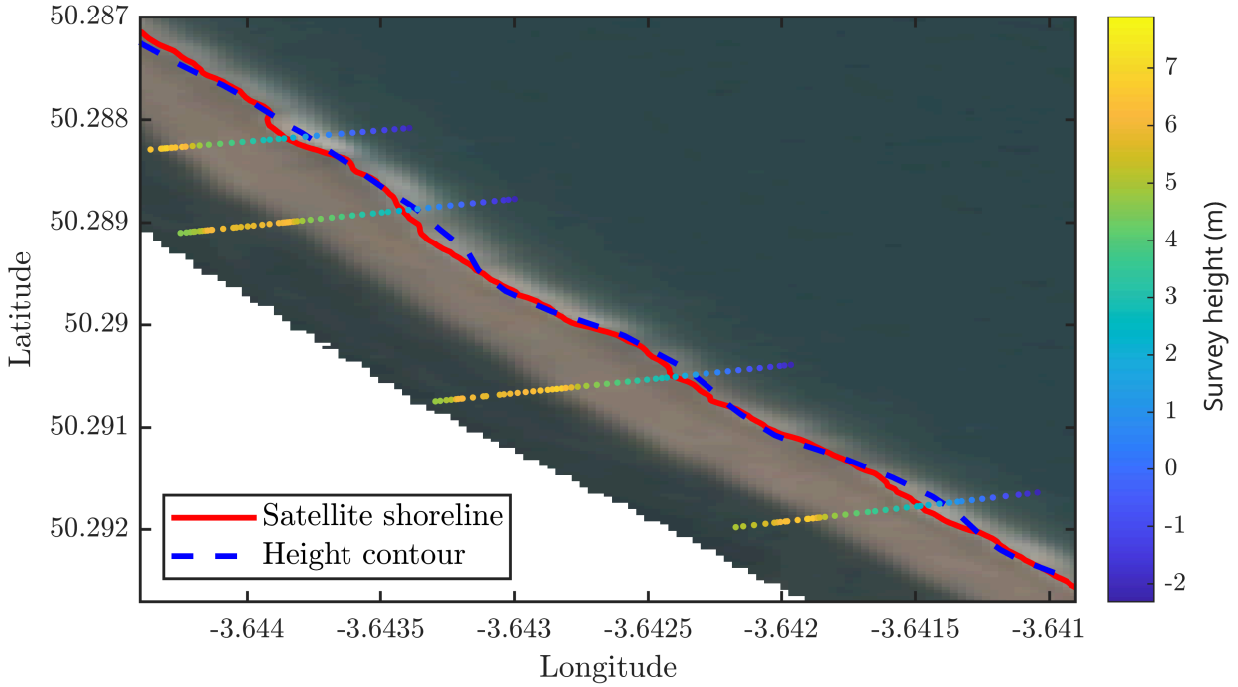



**Figure 9.** True colour image (TCI) of Start Bay alongside the satellite derived shoreline in red, the blue dashed line shows the height contour of the waterlevel at 1.52m, the intermittent transects show a survey at the site with the colour representing the topographic height with respect to the survey.

and obtained from the Channel Coastal Observatory (www.channelcoast.org) Channel Coastal Observatory (2025c). For each survey date, it was assumed that beach morphology remains relatively stable over a ±1 month window. Consequently, any PlanetScope image acquired within this two-month period was considered eligible for comparison. While this temporal window introduces potential uncertainty due to the dynamic nature of beach morphology, it was deemed necessary to ensure a sufficiently large sample size for the error distributions. This expanded window is critical for mitigating the influence of outliers, which are particularly prevalent in UK-based imagery datasets with cloud cover reaching up to 50%. To define the ground-truth shoreline, water level measurements from local tidal gauges were used in conjunction with the surveyed beach profiles to extract a height contour representing the still-water shoreline, based on a simplified bathtub model of tidal inundation.

This height contour was generated by first interpolating the survey data onto a regular grid using biharmonic spline interpolation. Castelle et al. (2015) demonstrated that inappropriate interpolation schemes can introduce spurious cuspate features in the derived shoreline. Biharmonic splines, being non-triangulation-based, were found to reduce these artefacts; however, some errors persisted in surveys with anisotropic transect spacing, which can degrade interpolation quality. While alternative methods such as anisotropic kriging have been proposed (Castelle et al., 2014), they require per-survey calibration and were not adopted in this study due to scalability concerns. Once the gridded topography was produced, a contour corresponding to the tidal level at the time of image acquisition was extracted and treated as the reference shoreline.

The tide height was taken as the local water level at the time of image acquisition, taken from the nearest appropriate tidal gauge. For Chesil this was Weymouth, Start Bay was Exmouth and Seaford-Brighton (British Oceanographic Data Centre, 2025; Channel Coastal Observatory, 2025b,a).

To facilitate direct comparison, this contour was discretised every 50 metres, with transects projected perpendicularly from this height contour. The error was then calculated as the horizontal distance between the satellite-derived shoreline and the corresponding point on the topographic contour along each transect. An example of this comparison is presented in Figure 9, where the satellite-derived shoreline (shown in red) is compared to the topographically derived contour (dashed blue), illustrating how spatial deviations are assessed.. This topographically derived contour is calculated by the interpolation of the survey transects, that are also marked in the figure.

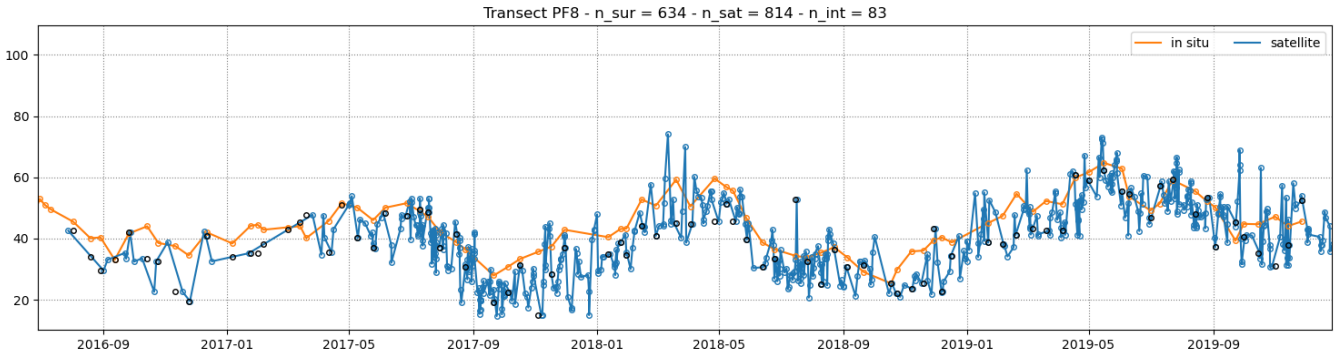



**Figure 10.** Comparison of the mean shoreline position using the Vos et al. (2023) workflow for Narrabeen beach. The Orange line shows in-situ survey, the blue line shows the satellite derived shoreline position decomposed with respect to the water level. Black circles are points that are directly compared to the in-situ survey.

The method presented in this study, alongside the CoastSat algorithm, is also applied to Narrabeen Beach, Australia, using the benchmarking approach established by Vos et al. (2023). This validation follows the methodology outlined in Doherty et al. (2022), but ensures consistency by using the same image dataset for both methods, allowing for a direct and unbiased comparison.

Figure 10 presents an example of the comparison between the satellite-derived shoreline and the in-situ survey data for a single transect. For both the proposed method and CoastSat, the shoreline is defined as the intersection point between the transect and the shoreline contour, with the most seaward intersection point used to represent the shoreline position. This approach standardises the comparison and allows for a consistent evaluation of positional accuracy across methods.

## 3 RESULTS AND DISCUSSION

### UK Quantitative Performance

Figure 11 presents histograms of the horizontal distance errors between the satellite-derived shorelines and the corresponding ground-truth positions obtained from topographic surveys across the three study sites: Seaford, Chesil, and Start Bay. CoastSat could not be successfully run at Seaford due to the location of the beach on the border of both UTM zone 30N and 31N, disrupting the algorithm. To reduce the influence of extreme outliers, the $2^{nd}$ and $98^{th}$ percentiles have been excluded from the data. The histograms compare the performance of the Coast-O-Matic method (shown in blue) against the CoastSat method (shown in orange), providing a visual indication of each method's error distribution and central tendency.

Supporting these visual results, Table 2 summarises several key quantitative metrics used to evaluate the performance of both models. The Root Mean Squared Error (RMSE) and Standard Deviation (STD)

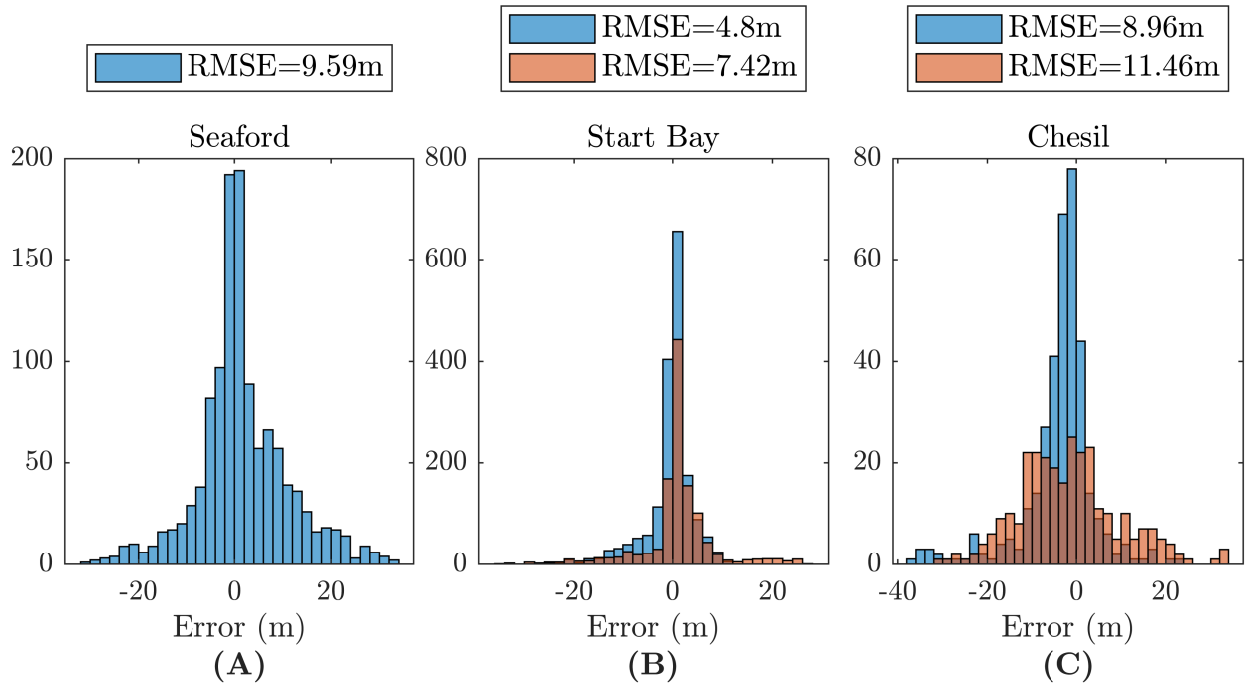



**Figure 11.** Histogram showing the mean distance between the satellite derived shoreline and the ground-truth shoreline, Blue is the Coast-O-Matic method and Orange is the CoastSat method, for **(A)** Seaford, **(B)** Start Bay and **(C)** Chesil.

are calculated from the average shoreline position, derived at $50\,\mathrm{m}$ intervals along each image transect. The values reported in the table represent the mean RMSE and STD across all valid images, reflecting the overall accuracy and variability of each method.

Both methods exhibit similarly shaped peaks in their error distributions, as seen in Figure 11, which suggests that for high-quality imagery, the two approaches produce comparable shoreline positions. This reflects the fundamental accuracy of both solvers under optimal conditions. However, the broader distribution of errors observed for CoastSat highlights the relative advantage of the Coast-O-Matic workflow, particularly its ability to automatically filter out anomalous or errant shoreline extractions prior to post-processing. This distinction is further supported by the lower RMSE and STD values reported for Coast-O-Matic in Table 2, where a significant driver of variability is the presence of outlier errors exceeding $20\,\mathrm{m}$.

**Table 2.** Comparison of shoreline extraction metrics between Coast-O-Matic and CoastSat across three sites.

| Site | Method | RMSE (m) | STD (m) | No. Dates | Intra-Image Mean STD (m) |
|---|---|---|---|---|---|
| Seaford | Coast-O-Matic | 9.59 | 9.46 | 1065 | 15.04 |
| | CoastSat | - | - | - | - |
| Start Bay | Coast-O-Matic | 4.80 | 4.70 | 877 | 5.96 |
| | CoastSat | 7.42 | 7.36 | 780 | 9.12 |
| Chesil | Coast-O-Matic | 8.96 | 10.92 | 1054 | 10.90 |
| | CoastSat | 11.46 | 11.34 | 1018 | 24.77 |

While it is theoretically possible to reduce such outliers in CoastSat by tightening the reference shoreline buffer, doing so would limit the method's applicability in more variable environments, such as low-sloping beaches or regions with large tidal ranges, where shoreline positions may deviate significantly from the reference.

The robustness of the extraction was assessed using the No. Dates metric, which represents the number of unique survey dates for which a valid shoreline was successfully derived. As shown in Table 2, Coast-O-Matic retrieved shorelines for a greater total number of dates than CoastSat at both comparable sites. This indicates that, overall, Coast-O-Matic is more robust: it successfully processes valid shoreline segments that might be rejected by rigid thresholding, while automatically suppressing regions with significant cloud or shadow noise.

However, a specific limitation was observed during early morning acquisitions characterized by low solar elevation. Under these "dark" conditions, the spectral contrast is often insufficient for the classifier, leading to image exclusion. Despite this specific limitation in low-light scenarios, the method maintains a high temporal resolution, averaging approximately one shoreline every two days since 2018.

The final metric examined is the Intra-Image Mean Standard Deviation (STD), which measures the within-image variability of the satellite-derived shoreline relative to the ground-truth shoreline from the surveys. This metric captures how much the distance between the two shorelines fluctuates across a single image, providing insight into the spatial consistency of the shoreline extraction. This metric highlights how smooth or spatially coherent the shoreline appears within a single scene.

Importantly, the intra-image STD is influenced by two primary sources of error: the spatial variation in the satellite-derived shoreline itself, and interpolation artefacts associated with the ground-truth topographic data. However, a key advantage of this metric is that it is insensitive to absolute geolocation errors, as such shifts would manifest uniformly across the image and not affect the internal variability. As a result, it offers a clearer view of local inconsistencies, independent of satellite positioning accuracy.

A notable difference is observed between the two methods in this metric, with CoastSat exhibiting substantially higher intra-image variability. At first glance, this is surprising, given that the CoastSat workflow includes a smoothing step specifically intended to regularise the extracted shoreline. This process should, in theory, reduce intra-image noise—though at the expense of spatial sensitivity, especially in heterogeneous environments. While smoothing is likely beneficial along continuous sandy beaches, it may obscure meaningful shoreline variation in areas with cliffs, headlands, or rocky outcrops, where spatial detail is important.

However, the elevated intra-image STD observed in CoastSat is explained by the presence of erroneous shoreline segments, introduced by image artefacts such as cloud cover, shadows, or surface glare. These artefacts can distort portions of the shoreline, inflating the measured standard deviation within the image. In such cases, the metric is not reflecting natural topographic variation, but rather localised error spikes caused by imperfect image conditions or misclassification. This highlights the need for effective quality control and filtering to ensure robust shoreline extractions, particularly in datasets with varying atmospheric and lighting conditions.

## Narrabeen Quantitative Performance

To further validate the proposed method, satellite-derived shorelines were generated for Narrabeen Beach, Australia, and assessed using the benchmarking framework established by Vos et al. (2023). The satellite-derived shorelines were compared to the intersection of the transect and the tidally corrected topographic

contour, with the shoreline defined as the first point of intersection along the transect. Consistent with the UK validation, the results were subjected to temporal filtering to remove extreme outliers: for any given point, the $1^{st}$ and $99^{th}$ percentiles were removed, and positions falling outside three standard deviations of a window, including the preceding 10 points and following 10 points, were excluded.

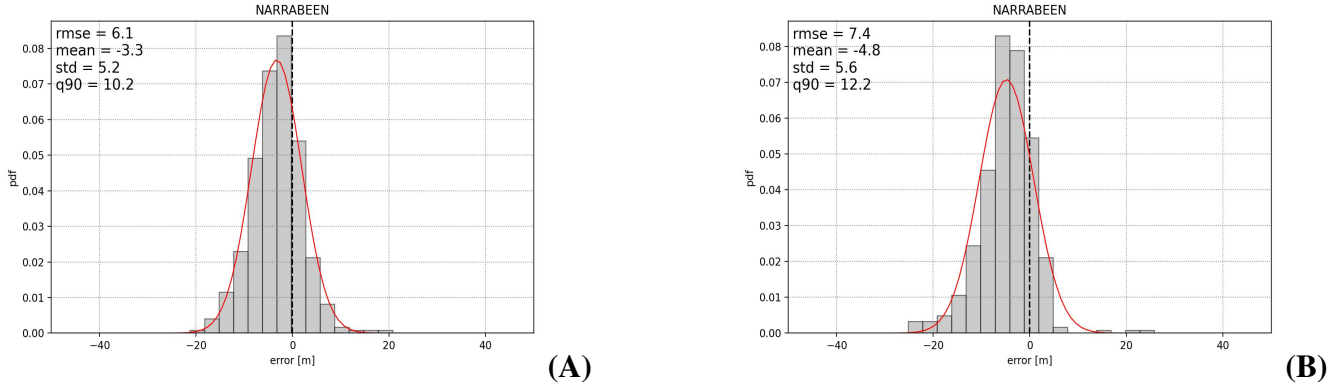



**Figure 12.** The results using the Vos et al. (2023) workflow for Narrabeen beach, when using a manual threshold filter. **(A)** Results for the Coast-O-Matic workflow. **(B)** Results for CoastSat.

Figure 12 presents the comparative results after applying a manual quality control threshold to remove gross outliers visible to the eye. In this filtered context, both methods demonstrate comparable accuracy: Coast-O-Matic achieves an RMSE of $6.1\,\mathrm{m}$ , while CoastSat achieves $7.4\,\mathrm{m}$. These values are consistent with the sub-pixel accuracy observed in the UK dataset and align with previous findings by Doherty et al. (2022) .

However, a critical distinction lies in the level of supervision required to achieve these results. The histograms in Figure 12 represent the ”best-case” scenario for CoastSat, where erroneous shorelines caused by cloud and shadow artifacts were manually identified and removed. Without this manual supervision—relying solely on the automated algorithm—CoastSat yielded an RMSE of $37.9\,\mathrm{m}$, driven by significant outliers where the threshold-based method misidentified cloud edges or offshore features as the shoreline. In contrast, the Coast-O-Matic method proved robust even prior to manual filtering, yielding an automated RMSE of $8.7\,\mathrm{m}$.

The disparity in automated performance is attributed to the challenging nature of the dataset used in this study, which includes higher cloud cover and variable lighting conditions compared to previous benchmarks. Additionally, the use of a larger $100\,\mathrm{m}$ buffer (compared to the standard $40\,\mathrm{m}$) increased the search space, exposing the threshold-based classifier to more potential non-shoreline boundaries. While CoastSat matches the proposed method’s accuracy under supervised conditions, its reliance on manual intervention or aggressive statistical filtering limits its utility for fully automated, large-scale monitoring. Aggressive statistical post-processing runs the risk of eliminating valid morphological changes, such as the formation of ephemeral bars or storm responses, which may statistically resemble outliers. Therefore, the inherent stability of the Coast-O-Matic probability classifier offers a significant advantage for operational coastal monitoring.

## 3.1 Constraints and Biases

The probabilistic method introduced in this study serves as a representative proxy for the shoreline rather than a strict delineation of the instantaneous waterline. A key component of the classification is

the "shallow water" class, which captures the high-variance zone at the land–sea interface. However, the reliance on spectral standard deviation calculated within a moving window (specifically at the $5 \times 5$ scale) introduces a theoretical landward bias. As the window traverses the shoreline, it incorporates high-contrast pixels from the adjacent beach, potentially extending the high-variance zone inland.

This effect aligns with the conceptual distinction between the waterline (the instantaneous water edge) and the wetline (the limit of saturated sand), as discussed by Pardo-Pascual et al. (2024). Since the classifier's high-variance zone spans both nearshore water and wet sand, the resulting shoreline is effectively drawn between these two boundaries. While larger windows exaggerate this shift by capturing more surrounding variance, the proposed ensemble framework mitigates this bias. By averaging the $5 \times 5$ output with the higher-precision $3 \times 3$ branch and the conservative binary classifier, the ensemble successfully anchors the shoreline, preventing significant landward drift as evidenced by the high accuracy observed in the UK and Narrabeen quantitative results.

This aggregation strategy may, however, present challenges in narrow fringing beach environments, specifically where the beach width is fewer than five pixels ($< 20\,\mathrm{m}$). In such restricted geometries, the $5 \times 5$ window risks encompassing non-beach elements—such as vegetation or urban infrastructure—which could inflate variance values. This noise creates a potential for land pixels to be misclassified as sea, drawing the shoreline landward toward the vegetation boundary rather than the true water interface. While the multi-branch architecture provides resilience, the method may be less stable in these constrained settings compared to wider, open coasts.

## 3.2 Qualitative Results

Beyond quantitative accuracy, the utility of the method is defined by its ability to resolve complex coastal features in environments that challenge traditional thresholding. Figure 13A displays Truc-Vert Beach, France, a site characterised by rhythmic shoreline structures such as embayments and rip channels (Castelle et al. (2015)). The satellite-derived shoreline clearly delineates these features, demonstrating that the 3.7 m resolution of PlanetScope imagery is sufficient for mapping small-scale nearshore variability. This robustness extends to surface heterogeneity, as seen in Figure 13B at the Drigg coast, Cumbria. As noted by Woombs (2021), this site contains patches of cobbles and stone that appear as dark regions above the waterline. While such variations often confuse simple thresholding algorithms, the Coast-O-Matic workflow successfully identifies the correct boundary, confirming that the probabilistic approach effectively utilises comprehensive spectral information beyond simple reflectance.

Despite these capabilities, a final operational limitation concerns illumination. The workflow is robust to discrete cloud shadows, as evidenced by the masking workflow, but it struggles with systemic low-light conditions. This includes images taken during early morning low solar elevation ("dark images") or significant topographic shading, such as that caused by west-facing cliffs at Chesil Beach. In the latter case, the morning acquisition time (10:00–11:00 local time) causes cliffs to cast shadows over the back-beach, reducing spectral reflectance to levels where information is unrecoverable, unlike the partial transparency of cloud shadows.

Finally, incorporating the standard deviation of a moving window served to reduce computational overhead by acting as a pre-filter. By limiting detailed classification to regions of high variance near the shoreline, the model achieved a significant reduction in runtime. The full dataset was processed in 7 hours, compared to 13 hours for the CoastSat model, without requiring additional data storage or high-performance computing infrastructure.

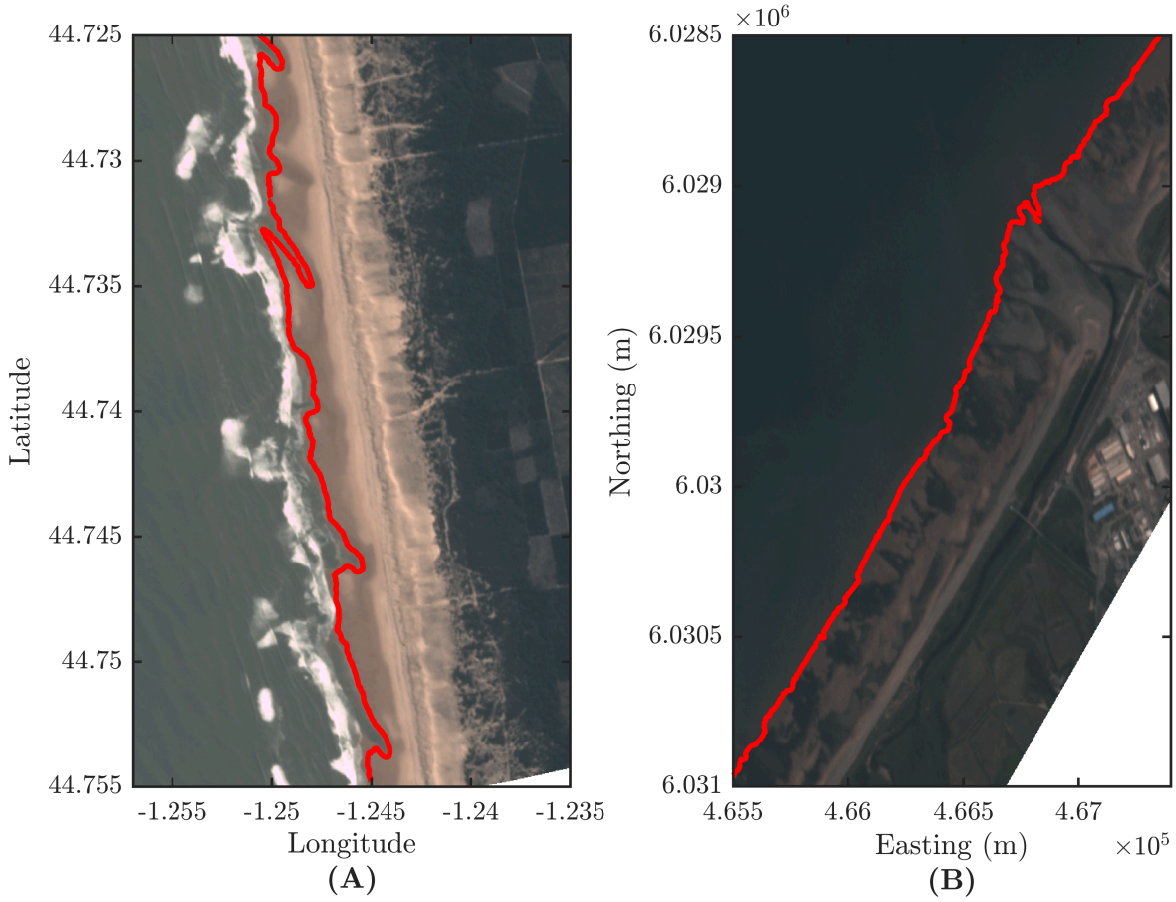



**Figure 13.** Shows the results of the Coast-O-Matic workflow for two different locations, with the satellite derived shoreline shown in red. **(A)** the true colour image (TCI) of Truc Vert beach, charcterised by it's rip channels. **(B)** the true colour image (TCI) of Cumbria, with it's exposed rock and clay beach.

## 4 CONCLUSION

Traditional methods that discretise the shoreline based on a single spectral index threshold have likely reached the upper limit of their achievable accuracy, particularly when applied to noisy or heterogeneous satellite imagery. The core limitation of such approaches lies not in the pixel-wise classification itself, but in the inability of a single index to consistently and accurately represent the waterline across spatially variable environments. This shortcoming becomes especially pronounced in coastal regions characterised by complex surface types, variable lighting, or mixed land cover.

In contrast, shoreline extraction based on probability isolines offers a more adaptable and robust framework. By using continuous probability fields, this approach decouples shoreline delineation from rigid spectral rules, and instead ties accuracy to the performance of the underlying classification model. As a result, improvements in pixel-level classification directly translate into higher precision shoreline estimates, including sub-pixel resolution when sufficient image quality and model confidence are achieved.

The ability to generalise across variable ground conditions is a key strength of the model, significantly reducing the need for retraining in different environmental contexts. Notably, all results presented in this study were generated using the same trained model, without site-specific tuning.

This workflow also emphasises shoreline stability and quality control, particularly through the removal of false positives. The model is designed under the assumption that omitting a shoreline is preferable to incorrectly identifying one, an approach that improves reliability in operational or automated workflows. As previously discussed, in favourable image conditions, the method performs similarly to conventional threshold-based models. However, under challenging conditions, such as low visibility or heterogeneous land cover, many existing algorithms are prone to detecting erroneous boundaries caused by image noise or misclassification of non-coastal features.

This paper has presented the results of the Coast-O-Matic workflow at several locations and highlights a number of advantages of this methodology:

- A shoreline detection accuracy of under 3 pixels even when using a dataset containing images with a cloud cover up to 50%.
- A generalised approach that works on heterogenous coasts, without need for site specific tuning.
- An adaptive masking method that automatically filters anomalous shorelines prior to post-processing, reducing the influence of outliers.
- A computational performance increase, with lower computational storage requirements and faster run-times.

With the continued development and integration of advanced computer vision techniques, the error associated with pixel classification is steadily decreasing. The method introduced in this study is designed to leverage these advances, offering a flexible and scalable workflow capable of producing high-resolution, consistent shoreline estimates across diverse environmental conditions. Crucially, the framework preserves the potential for sub-pixel shoreline detection while addressing the limitations of traditional threshold-based approaches.

## CONFLICT OF INTEREST STATEMENT

The authors declare that the research was conducted in the absence of any commercial or financial relationships that could be construed as a potential conflict of interest.

## AUTHOR CONTRIBUTIONS

AH: Conceptualization, Methodology, Software, Investigation, Writing – original draft. JL: Supervision, Funding acquisition, Writing – review & editing. IK: Supervision, Funding acquisition, Writing – review & editing.

## FUNDING

This research was funded by Radioactive Waste Management Ltd, trading as Nuclear Waste Services, via the Nuclear Waste Services Research Support Office (RWM167), project code RWM602.

## ACKNOWLEDGMENTS

Tide gauge data for Weymouth were supplied by the British Oceanographic Data Centre (BODC) as part of the UK National Tide Gauge Network, owned and operated by the Environment Agency. Data for Brighton Marina were collected by the Southeast Regional Coastal Monitoring Programme and provided

courtesy of the Channel Coastal Observatory. Data for Exmouth were collected by the Southwest Regional Coastal Monitoring Programme and provided courtesy of the Channel Coastal Observatory. All UK coastal monitoring data were provided by the National Network of Regional Coastal Monitoring Programmes of England and the Wales Coastal Monitoring Centre, managed and distributed by the Channel Coastal Observatory. The data are available under the Open Government Licence.

## DATA AVAILABILITY STATEMENT

The source code for the Coast-O-Matic algorithm, including the Planet API retrieval pipeline and AROSICS-based co-registration with ESRI basemaps, is available at: https://github.com/AlfieHewetson/Coast-O-Matic.

## REFERENCES

Abdelhady, H. U., Troy, C. D., Habib, A., and Manish, R. (2022). A simple, fully automated shoreline detection algorithm for high-resolution multi-spectral imagery. *Remote Sensing* 14, 557. doi:10.3390/rs14030557

Almeida, L. P., de Oliveira, I. E., Lyra, R., Dazzi, R. L. S., Martins, V. G., and da Fontoura Klein, A. H. (2021). Coastal analyst system from space imagery engine (cassie): Shoreline management module. *Environmental Modelling & Software* 140, 105033. doi:10.1016/J.ENVSOFT.2021.105033

Angelini, R., Angelats, E., Luzi, G., Masiero, A., Simarro, G., and Ribas, F. (2024). Development of methods for satellite shoreline detection and monitoring of megacusp undulations. *Remote Sensing* 16, 4553. doi:10.3390/rs16234553

Angelini, R., Angelats, E., Ribas, F., Luzi, G., Di Ciaccio, F., Mugnai, F., et al. (2025). Enhanced SAR-based shoreline extraction in microtidal beaches through improved preprocessing of Sentinel-1 and TerraSAR-X data. *IEEE Journal of Selected Topics in Applied Earth Observations and Remote Sensing* 18, 23658–23673. doi:10.1109/JSTARS.2024.3411030

Belward, A. S. and Skøien, J. O. (2015). Who launched what, when and why; trends in global land-cover observation capacity from civilian earth observation satellites. *ISPRS Journal of Photogrammetry and Remote Sensing* 103, 115–128. doi:10.1016/J.ISPRSJPRS.2014.03.009

Bishop-Taylor, R., Sagar, S., Lymburner, L., Alam, I., and Sixsmith, J. (2019). Sub-pixel waterline extraction: Characterising accuracy and sensitivity to indices and spectra. *Remote Sensing 2019, Vol. 11, Page 2984* 11, 2984. doi:10.3390/RS11242984

Boak, E. H. and Turner, I. L. (2005). Shoreline definition and detection: A review. *Journal of Coastal Research* 21, 688–703. doi:10.2112/03-0071.1

Braun, A. (2021). Retrieval of digital elevation models from sentinel-1 radar data - open applications, techniques, and limitations. *Open Geosciences* 13, 532–569. doi:10.1515/GEO-2020-0246/MACHINEREADABLECITATION/RIS

[Dataset] British Oceanographic Data Centre (2025). UK National Tide Gauge Network: Weymouth [Data set]. Available at: `https://www.bodc.ac.uk/data/hosted_data_systems/sea_level/uk_tide_gauge_network/`. Data for 1991–2024. Funded by the Environment Agency. Accessed: 2025-10-25

Castelle, B., Marieu, V., Bujan, S., Ferreira, S., Parisot, J. P., Capo, S., et al. (2014). Equilibrium shoreline modelling of a high-energy meso-macrotidal multiple-barred beach. *Marine Geology* 347, 85–94. doi:10.1016/J.MARGEO.2013.11.003

Castelle, B., Marieu, V., Bujan, S., Splinter, K. D., Robinet, A., Senechal, N., et al. (2015). On the impact of a series of severe storms on a double-barred sandy coast: Dune erosion and megacups embayments. In *The Proceedings of the Coastal Sediments 2015* (San Diego, USA: World Scientific). doi:10.1142/9789814689977_0259

[Dataset] Channel Coastal Observatory (2025a). Brighton Marina Tide Gauge Data [Data set]. Available at: `https://www.channelcoast.org/`. Data covering 2018–2024. Accessed: 2025-07-07

[Dataset] Channel Coastal Observatory (2025b). Exmouth Marina Tide Gauge Data [Data set]. Available at: `https://www.channelcoast.org/`. Data covering 2015–2024. Managed by Teignbridge District Council. Accessed: 2025-07-07

[Dataset] Channel Coastal Observatory (2025c). National Network of Regional Coastal Monitoring Programmes: England and Wales Topographic and Bathymetric Surveys [Data set]. Available at: `https://coastalmonitoring.org/`. Includes data from the Northeast, East Riding, Anglian, Southeast, Southwest, Northwest, and Wales Regional Programmes. Accessed: 2025-12-05

Cipolletti, M. P., Delrieux, C. A., Perillo, G. M., and Piccolo, M. C. (2012). Superresolution border segmentation and measurement in remote sensing images. *Computers & Geosciences* 40, 87–96. doi:10.1016/J.CAGEO.2011.07.015

Collison, A., Jumpasut, A., and Bourne, H. (2022). *On-Orbit Radiometric Calibration of the Planet Satellite Fleet Doves and SkySats*. White paper, Planet Labs PBC, San Francisco, CA

da Silva, P. G., Jara, M. S., Medina, R., Beck, A. L., and Taji, M. A. (2024). On the use of satellite information to detect coastal change: Demonstration case on the coast of spain. *Coastal Engineering* 191, 104517. doi:10.1016/J.COASTALENG.2024.104517

Di, L. and Yu, E. (2023). Remote sensing. In *Remote Sensing Big Data* (Cham: Springer). 17–43. doi:10.1007/978-3-031-33932-5_2

Dobrinić, D., Gašparović, M., and Župan, R. (2018). Horizontal accuracy assessment of planetscope, rapideye and worldview-2 satellite imagery. *International Multidisciplinary Scientific GeoConference Surveying Geology and Mining Ecology Management, SGEM* 18, 129–136. doi:10.5593/SGEM2018/2.3/S10.017

Doherty, Y., Harley, M. D., Vos, K., and Splinter, K. D. (2022). A python toolkit to monitor sandy shoreline change using high-resolution planetscope cubesats. *Environmental Modelling and Software* 157. doi:10.1016/J.ENVSOFT.2022.105512

Dolan, R., Hayden, B., and Heywood, J. (1978). A new photogrammetric method for determining shoreline erosion. *Coastal Engineering* 2, 21–39. doi:10.1016/0378-3839(78)90003-0

[Dataset] ESA Space Solutions (2020). Newcomers earth observation guide. Version 1.9. Accessed: 2025-09-14

[Dataset] Esri (2025). World imagery (mapserver) tile service. ArcGIS REST Services Directory. Attribution on service: Source: Esri, Maxar, Earthstar Geographics, and the GIS User Community

Feyisa, G. L., Meilby, H., Fensholt, R., and Proud, S. R. (2014). Automated water extraction index: A new technique for surface water mapping using landsat imagery. *Remote Sensing of Environment* 140, 23–35. doi:10.1016/J.RSE.2013.08.029

Frazier, A. E. and Hemingway, B. L. (2021). A technical review of planet smallsat data: Practical considerations for processing and using planetscope imagery. *Remote Sensing 2021, Vol. 13, Page 3930* 13, 3930. doi:10.3390/RS13193930

[Dataset] Gafford, J. (2026). Multi-Layer Perceptron (MLP) Class. MATLAB Central File Exchange. Accessed: February 21, 2026

García-Rubio, G., Huntley, D., and Russell, P. (2015). Evaluating shoreline identification using optical satellite images. *Marine Geology* 359, 96–105. doi:10.1016/J.MARGEO.2014.11.002

Geudtner, D., Torres, R., Snoeij, P., Davidson, M., and Rommen, B. (2014). Sentinel-1 system capabilities and applications. *International Geoscience and Remote Sensing Symposium (IGARSS)* , 1457–1460doi:10.1109/IGARSS.2014.6946711

Hagenaars, G., de Vries, S., Luijendijk, A. P., de Boer, W. P., and Reniers, A. J. (2018). On the accuracy of automated shoreline detection derived from satellite imagery: A case study of the sand motor mega-scale nourishment. *Coastal Engineering* 133, 113–125. doi:10.1016/J.COASTALENG.2017.12.011

Harley, M. D., Kinsela, M. A., Sánchez-García, E., and Vos, K. (2019). Shoreline change mapping using crowd-sourced smartphone images. *Coastal Engineering* 150, 175–189. doi:10.1016/J.COASTALENG.2019.04.003

Houborg, R. and McCabe, M. F. (2018). A cubesat enabled spatio-temporal enhancement method (cestem) utilizing planet, landsat and modis data. *Remote Sensing of Environment* 209, 211–226. doi:10.1016/J.RSE.2018.02.067

Huang, H. and Roy, D. P. (2021). Characterization of planetscope-0 planetscope-1 surface reflectance and normalized difference vegetation index continuity. *Science of Remote Sensing* 3, 100014. doi:10.1016/J.SRS.2021.100014

Kalacska, M., Arroyo-Mora, J. P., Coomes, O. T., Takasaki, Y., and Abizaid, C. (2022). Multi-temporal surface water classification for four major rivers from the peruvian amazon. *Data 2022, Vol. 7, Page 6* 7, 6. doi:10.3390/DATA7010006

Keay, L., Mulverhill, C., Coops, N. C., and McCartney, G. (2023). Automated forest harvest detection with a normalized planetscope imagery time series. *Canadian Journal of Remote Sensing* 49. doi:10.1080/07038992.2022.2154598

Kelly, J. T. and Gontz, A. M. (2019). Rapid assessment of shoreline changes induced by tropical cyclone oma using cubesat imagery in southeast queensland, australia. *https://doi.org/10.2112/JCOASTRES-D-19-00055.1* 36, 72–87. doi:10.2112/JCOASTRES-D-19-00055.1

Konstantinou, A., Scott, T., Masselink, G., Stokes, K., Conley, D., and Castelle, B. (2023). Satellite-based shoreline detection along high-energy macrotidal coasts and influence of beach state. *Marine Geology* 462, 107082. doi:10.1016/J.MARGEO.2023.107082

Kriegler, F., Malila, W., Nalepka, R., and Richardson, W. (1969). Preprocessing transformations and their effects on multspectral recognition. *Proceedings of the Sixth International Symposium on Remote Sesning of Environment* , 97–131

Kulpa, Z. (1983). More about areas and perimeters of quantized objects. *Computer Vision, Graphics, and Image Processing* 22, 268–276. doi:10.1016/0734-189X(83)90069-5

Lamquin, N., Woolliams, E., Bruniquel, V., Gascon, F., Gorroño, J., Govaerts, Y., et al. (2019). An inter-comparison exercise of sentinel-2 radiometric validations assessed by independent expert groups. *Remote Sensing of Environment* 233, 111369. doi:10.1016/J.RSE.2019.111369

Larson, M. and Kraus, N. C. (1994). Temporal and spatial scales of beach profile change, duck, north carolina. *Marine Geology* 117, 75–94. doi:10.1016/0025-3227(94)90007-8

Li, W. and Gong, P. (2016). Continuous monitoring of coastline dynamics in western florida with a 30-year time series of landsat imagery. *Remote Sensing of Environment* 179, 196–209. doi:10.1016/J.RSE.2016.03.031

Luijendijk, A., Hagenaars, G., Ranasinghe, R., Baart, F., Donchyts, G., and Aarninkhof, S. (2018). The state of the world's beaches. *Scientific Reports 2018 8:1* 8, 1–11. doi:10.1038/s41598-018-24630-6

Mao, Y., Harris, D. L., Xie, Z., and Phinn, S. (2021). Efficient measurement of large-scale decadal shoreline change with increased accuracy in tide-dominated coastal environments with google earth engine. *ISPRS Journal of Photogrammetry and Remote Sensing* 181, 385–399. doi:10.1016/J.ISPRSJPRS.2021.09.021

Markham, B., Barsi, J., Kvaran, G., Ong, L., Kaita, E., Biggar, S., et al. (2014). Landsat-8 operational land imager radiometric calibration and stability. *Remote Sensing 2014, Vol. 6, Pages 12275-12308* 6, 12275–12308. doi:10.3390/RS61212275

Mason, D. C., Davenport, I. J., Robinson, G. J., Flather, R. A., and McCartney, B. S. (1995). Construction of an inter-tidal digital elevation model by the 'water-line' method. *Geophysical Research Letters* 22, 3187–3190. doi:10.1029/95GL03168

McCarroll, R. J., Valiente, N. G., Wiggins, M., Scott, T., and Masselink, G. (2023). Coastal survey data for perranporth beach and start bay in southwest england (2006–2021). *Scientific Data 2023 10:1* 10, 1–17. doi:10.1038/s41597-023-02131-0

McFeeters, S. K. (1996). The use of the normalized difference water index (ndwi) in the delineation of open water features. *International Journal of Remote Sensing* 17, 1425–1432. doi:10.1080/01431169608948714

Muis, S., Apecechea, M. I., Dullaart, J., de Lima Rego, J., Madsen, K. S., Su, J., et al. (2020). A high-resolution global dataset of extreme sea levels, tides, and storm surges, including future projections. *Frontiers in Marine Science* 7, 512955. doi:10.3389/FMARS.2020.00263

Otsu, N. (1979). Threshold selection method from gray-level histograms. *IEEE Trans Syst Man Cybern* SMC-9, 62–66. doi:10.1109/TSMC.1979.4310076

Palomar-Vázquez, J., Almonacid-Caballer, J., Pardo-Pascual, J. E., and Sánchez-García, E. (2018). SHOREX: A new tool for automatic and massive extraction of shorelines from Landsat and Sentinel-2 imagery. In *Proceedings of the 7th International Conference on the Application of Physical Modelling in Coastal and Port Engineering and Science (Coastlab18)* (Santander, Spain)

Pardo-Pascual, J. E., Almonacid-Caballer, J., Cabezas-Rabadán, C., Fernández-Sarría, A., Armaroli, C., Ciavola, P., et al. (2024). Assessment of satellite-derived shorelines automatically extracted from sentinel-2 imagery using saet. *Coastal Engineering* 188, 104426. doi:10.1016/J.COASTALENG.2023.104426

Pardo-Pascual, J. E., Almonacid-Caballer, J., Ruiz, L. A., Palomar-Vázquez, J., and Rodrigo-Alemany, R. (2014). Evaluation of storm impact on sandy beaches of the gulf of valencia using Landsat imagery series. *Geomorphology* 214, 388–401. doi:10.1016/j.geomorph.2014.02.020

[Dataset] PBC, P. L. (2021). Do you provide relative spectral response curves (rsrs) for your satellites? Planet Support article; attached file: dove_r.csv. Last updated March 24, 2021

Phiri, D., Simwanda, M., Salekin, S., Nyirenda, V. R., Murayama, Y., and Ranagalage, M. (2020). Sentinel-2 data for land cover/use mapping: A review. *Remote Sensing 2020, Vol. 12, Page 2291* 12, 2291. doi:10.3390/RS12142291

Planet Labs PBC (2023). *Planet Imagery Product Specifications*. Planet Labs PBC, San Francisco, CA

[Dataset] Rouse Jr, J. W., Haas, R. H., Deering, D., Schell, J., and Harlan, J. C. (1974). Monitoring the vernal advancement and retrogradation (green wave effect) of natural vegetation

Roy, D. P., Huang, H., Houborg, R., and Martins, V. S. (2021). A global analysis of the temporal availability of planetscope high spatial resolution multi-spectral imagery. *Remote Sensing of Environment* 264, 112586. doi:10.1016/J.RSE.2021.112586

Rustamov, R. B., Hasanova, S., and Zeynalova, M. H. (eds.) (2018). *Multi-purposeful Application of Geospatial Data* (InTechOpen). doi:10.5772/intechopen.69713

Safyan, M. (2020). Planet's dove satellite constellation. *Handbook of Small Satellites* , 1–17doi:10.1007/978-3-030-20707-6_64-1

Salameh, E., Frappart, F., Turki, I., and Laignel, B. (2020). Intertidal topography mapping using the waterline method from sentinel-1 & -2 images: The examples of arcachon and veys bays in france. *ISPRS Journal of Photogrammetry and Remote Sensing* 163, 98–120. doi:10.1016/J.ISPRSJPRS.2020.03.003

Savastano, S., Gomes da Silva, P., Sánchez, J. M., Tort, A. G., Payo, A., Pattle, M. E., et al. (2024). Assessment of shoreline change from SAR satellite imagery in three tidally controlled coastal environments. *Journal of Marine Science and Engineering* 12, 163. doi:10.3390/jmse12010163

Scheffler, D., Hollstein, A., Diedrich, H., Segl, K., and Hostert, P. (2017). Arosics: An automated and robust open-source image co-registration software for multi-sensor satellite data. *Remote Sensing 2017, Vol. 9, Page 676* 9, 676. doi:10.3390/RS9070676

Scott, T., Masselink, G., and Russell, P. (2011). Morphodynamic characteristics and classification of beaches in england and wales. *Marine Geology* 286, 1–20. doi:10.1016/J.MARGEO.2011.04.004

Shanehsazzadeh, A. and Holmes, P. (2007). Field investigation on the results of non-linear shallow water equations in the swash zone. *Coastal Engineering* 54, 835–855. doi:10.1016/J.COASTALENG.2007.05.016

Splinter, K. D., Turner, I. L., and Davidson, M. A. (2013). How much data is enough? the importance of morphological sampling interval and duration for calibration of empirical shoreline models. *Coastal Engineering* 77, 14–27. doi:10.1016/J.COASTALENG.2013.02.009

Spoto, F., Sy, O., Laberinti, P., Martimort, P., Fernandez, V., Colin, O., et al. (2012). Overview of sentinel-2. *International Geoscience and Remote Sensing Symposium (IGARSS)* , 1707–1710doi:10.1109/IGARSS.2012.6351195

Torres, R., Snoeij, P., Geudtner, D., Bibby, D., Davidson, M., Attema, E., et al. (2012). Gmes sentinel-1 mission. *Remote Sensing of Environment* 120, 9–24. doi:10.1016/J.RSE.2011.05.028

Tu, Y. H., Johansen, K., Aragon, B., Hajj, M. M. E., and McCabe, M. F. (2022). The radiometric accuracy of the 8-band multi-spectral surface reflectance from the planet superdove constellation. *International Journal of Applied Earth Observation and Geoinformation* 114, 103035. doi:10.1016/J.JAG.2022.103035

Turner, I. L., Harley, M. D., Short, A. D., Simmons, J. A., Bracs, M. A., Phillips, M. S., et al. (2016). A multi-decade dataset of monthly beach profile surveys and inshore wave forcing at narrabeen, australia. *Scientific Data 2016 3:1* 3, 1–13. doi:10.1038/sdata.2016.24

Vantor (2024). *Use Cases: Powering Every Mission*. Tech. rep., Vantor. Accessed: 2026-02-18

Vitousek, S., Buscombe, D., Vos, K., Barnard, P. L., Ritchie, A. C., and Warrick, J. A. (2023). The future of coastal monitoring through satellite remote sensing. *Cambridge Prisms: Coastal Futures* 1. doi:10.1017/CFT.2022.4

Vos, K., Harley, M. D., Splinter, K. D., Simmons, J. A., and Turner, I. L. (2019). Sub-annual to multi-decadal shoreline variability from publicly available satellite imagery. *Coastal Engineering* 150, 160–174. doi:10.1016/J.COASTALENG.2019.04.004

Vos, K., Splinter, K. D., Palomar-Vázquez, J., Pardo-Pascual, J. E., Almonacid-Caballer, J., Cabezas-Rabadán, C., et al. (2023). Benchmarking satellite-derived shoreline mapping algorithms. *Communications Earth & Environment 2023 4:1* 4, 1–17. doi:10.1038/s43247-023-01001-2

Vossepoel, A. M. and Smeulders, A. W. (1982). Vector code probability and metrication error in the representation of straight lines of finite length. *Computer Graphics and Image Processing* 20, 347–364. doi:10.1016/0146-664X(82)90057-0

887 Vousdoukas, M. I., Mentaschi, L., Voukouvalas, E., Verlaan, M., Jevrejeva, S., Jackson, L. P., et al. (2018).
888 Global probabilistic projections of extreme sea levels show intensification of coastal flood hazard. *Nature*
889 *Communications* 9. doi:10.1038/s41467-018-04692-w
890 Williams, A. T., Rangel-Buitrago, N., Pranzini, E., and Anfuso, G. (2018). The management of coastal
891 erosion. *Ocean & Coastal Management* 156, 4–20. doi:10.1016/J.OCECOAMAN.2017.03.022
892 Wilson, N., Greenberg, J., Jumpasut, A., Collison, A., and Weichelt, H. (2017). Absolute radiometric
893 calibration of Planet Dove satellites, flocks 2p and 2e. In *Algorithms, Technologies, and Applications for*
894 *Multispectral and Hyperspectral Imagery XXIII* (SPIE), vol. 10205 of *Proceedings of SPIE*, 102050W.
895 doi:10.1117/12.2262590
896 [Dataset] Woombs, M. (2021). An intertidal survey of the biotopes of rocky scars in the drigg coast,
897 european marine site
898 Wulder, M. A., Roy, D. P., Radeloff, V. C., Loveland, T. R., Anderson, M. C., Johnson, D. M., et al.
899 (2022). Fifty years of landsat science and impacts. *Remote Sensing of Environment* 280, 113195.
900 doi:10.1016/J.RSE.2022.113195
901 Zhang, K., Douglas, B. C., and Leatherman, S. P. (2004). Global warming and coastal erosion. *Climatic*
902 *Change* 64, 41–58. doi:10.1023/B:CLIM.0000024690.32682.48/METRICS